Article Sur le critère de mélange homogène et les problèmes de consistance dans les modèles hybrides eulériens lagrangiens stochastiques de dispersion

Cet article a été soumis à *Atmospheric Environment*. Il développe tout d'abord la théorie de la modélisation de la dispersion lagrangienne stochastique. Il traite ensuite le problème du critère de mélange homogène, démontrant que le bon respect de celui-ci réside en la bonne introduction du terme de gradient de pression en tant que terme de dérive moyen de l'équation de Langevin. Sur ce sujet, des considérations d'ordre numérique sont abordées afin d'expliquer comment correctement implémenter le terme de gradient de pression dans la pratique et les difficultés numériques que cela peut engendrer. Ensuite, les questions de consistance entre champs eulérien et lagrangien sont développées. L'ensemble de ces points théoriques est supporté par des vérifications numériques couvrant un large panel d'applications pratiques.

Sommaire

5.1 Article

On the well-mixed condition and consistency issues in hybrid Eulerian/Lagrangian stochastic models of dispersion

Meïssam L. Bahlali[a], Christophe Henry[b], Bertrand Carissimo[a], Jean-Pierre Minier[c]

[a] *CEREA, Joint laboratory Ecole des Ponts ParisTech/EDF R&D, 6 quai Watier, 78401 Chatou Cedex, France*

[b] *Laboratoire Lagrange, Université de la Côte d'Azur, OCA, CNRS, 06304 Nice Cedex 4, France*

[c] *EDF R&D, MFEE, 6 quai Watier, 78401 Chatou Cedex, France*

Abstract

The purpose of the present article is to clarify issues related to the expression of Lagrangian stochastic models used for atmospheric dispersion applications. Two aspects are addressed: the respect of the well-mixed criterion and the correspondence between Eulerian and Lagrangian turbulence models when they are combined in practical simulations. Through theoretical and numerical considerations, it is first demonstrated that the fulfillment of the well-mixed criterion depends only on the proper incorporation of the mean pressure-gradient term as the mean drift term of the Langevin equation. In the second part of this work, consistency issues between duplicate fields within Eulerian/Lagrangian hybrid formulations are brought out. Such hybrid methods, where mean flow quantities calculated with an Eulerian approach are provided to a Lagrangian one, are commonly used in atmospheric dispersion simulations for their numerical efficiency. Nevertheless, it is shown that serious inconsistencies can result from coupling Eulerian and Lagrangian models that do not correspond to the same level of description of the fluid turbulence, thereby limiting the range of validity of some currently-used hybrid formulations.

Keywords: Turbulence, Stochastic modeling, Eulerian/Lagrangian methods, Well-mixed criterion, Consistency issues, Dispersion models

1. Introduction

Lagrangian stochastic models for atmospheric dispersion purposes have been studied extensively since the 1980s. These models reproduce advective transport in the atmosphere by explicitly tracking a large number of representative fluid particles where, usually, the evolution of particle velocities is driven by a stochastic differential equation of a Langevin type. First well-known references in Lagrangian stochastic modeling are, for example, Wilson et al. (1981); Van Dop et al. (1985); De Baas et al. (1986); Sawford (1985), or the classic paper Thomson (1987). In most of these works, the so-called 'well-mixed condition'

Email address: meissambahlali@gmail.com (Meïssam L. Bahlali)

issue was brought out as a challenging issue. First introduced by Sawford (1986), this issue corresponds to the thermodynamic constraint stating that an initially uniform distribution of particles (each representing an equal amount of mass) in an incompressible flow must remain uniform. The well-mixed criterion is a necessary criterion for any Lagrangian stochastic model to be regarded as acceptable since its violation means that density is no longer constant (therefore at variance with the incompressibility constraint). For that reason, various authors have tried to provide conditions to ensure that it is respected. Yet, how it has to be introduced or accounted for in specific Lagrangian stochastic models still needs further clarification.

Since the works mentioned above, significant improvements in Lagrangian stochastic modeling have been achieved in other fields where similar models are currently applied, in particular in turbulent combustion modeling (Pope, 1985, 1991), in single-phase flow turbulence modeling (Pope, 1994b) as well as in dispersed turbulent two-phase flows applications (Minier and Peirano, 2001; Minier, 2015). For instance, Pope (1987) showed that a necessary and sufficient condition for the well-mixed criterion to be fulfilled is that the calculated mean velocity field satisfies the continuity equation and that this condition is, in turn, equivalent to incorporating properly the mean pressure-gradient term in the Langevin model. However, in the recent atmospheric literature relative to Lagrangian dispersion modeling (see, *e.g.*, Franzese (2003); Stohl et al. (2005); Alessandrini and Ferrero (2009); Tinarelli et al. (2013)), the formulations introduced by Pope and referred to as 'PDF (Probability Density Function) methods' are not widely used. Cassiani et al. (2005a,b, 2007) referred to Pope's PDF framework for micro-mixing modeling but followed Thomson (1987)'s approach to close the fluctuating pressure gradient and viscous terms.

In this context, this paper aims at bridging the developments made in Lagrangian stochastic models in reactive and two-phase flows with atmospheric dispersion applications. It has a two-fold objective: (a) to clarify remaining confusions about the well-mixed condition; (b) to provide a better understanding of consistency issues between fields obtained from Eulerian and Lagrangian simulations when hybrid Eulerian/Lagrangian numerical formulations are used. More specifically, two points are brought out and supported by numerical applications:

(i) The respect of the well-mixed criterion depends only on the proper introduction of the mean pressure-gradient term as the mean drift component of the Langevin model, regardless of further details.

(ii) In so-called Eulerian/Lagrangian hybrid numerical formulations, such as the one considered in the present simulations, the mean fields corresponding to the first and second moments of the velocity field are duplicate fields and need to be regarded as such. In other words, identity between predictions of the Eulerian and Lagrangian solvers must be verified for a model and its numerical implementation to be acceptable.

This paper is organized as follows. In section 2, Lagrangian stochastic models for atmospheric dispersion are introduced and the formulation of the well-mixed condition, as

well as consistencies between duplicate turbulence models and wall-boundary conditions, are discussed. Numerical assessment of the respect of the well-mixed criterion through the simple introduction of the mean pressure gradient is detailed in section 3, through three simulations of non-homogeneous turbulent flows that cover a wide range of practical situations. The consistency issue between Eulerian and Lagrangian turbulence models is addressed in section 5 before reaching conclusions.

2. Theoretical background on particle stochastic methods

2.1. Introduction to the well-mixed condition problem

In particle-based methods, a fluid flow is represented by tracking a large number of (fluid) particles. These particles can be seen as small 'frozen' amount of mass being transported with the flow or as points (to which a given mass is assigned) moving through a domain. Depending on the issue being addressed, different variables can be attached to particles, such as temperature, scalar values (either passive or reactive), compositions, etc., but the flow dynamics is always captured by explicitly tracking particle positions and velocities. For turbulent flows, when only reduced information, such as one-point statistics (*e.g.*, mean fluid velocities, kinetic energy, etc.), are needed, particle dynamics is often modeled by replacing the exact dynamics by a stochastic model. Then, the application of Kolmogorov theory to Lagrangian statistics for high Reynolds-number flows suggests to use a stochastic diffusion process for the evolution of fluid-particle velocities. The rationale and details leading to such formulations have been addressed at length elsewhere and readers are referred to existing comprehensive reviews for more details on this subject (Monin and Yaglom, 1971; Pope, 1985, 1994a, 2000; Minier and Peirano, 2001; Minier, 2016).

The basis of Lagrangian stochastic models for atmospheric studies consists therefore in describing fluid particle locations $\mathbf{X}_p(t)$ and velocities $\mathbf{U}_p(t)$ using the general formulation:

$$dX_{p,i} = U_{p,i}\,dt\ , \tag{1a}$$

$$dU_{p,i} = a_i(\mathbf{X}_p(t), \mathbf{U}_p(t), t)\,dt + b_{ij}(\mathbf{X}_p(t), \mathbf{U}_p(t), t)\,dW_j\ , \tag{1b}$$

where dW_j are independent Wiener processes. Briefly speaking, a Wiener process is a Gaussian process with independent increments of zero mean and with a variance equal to dt (more details can be found in Gardiner (1985); Öttinger (1996)). Eqs. (1) represent the stochastic differential equations (SDEs) for the trajectories of the stochastic process $(\mathbf{X}_p(t), \mathbf{U}_p(t))$.

In the weak sense, this is equivalent to considering particles as samples of a PDF whose evolution is determined by a partial differential equation (PDE), namely the Fokker-Planck equation which writes:

$$\frac{\partial f}{\partial t} + \frac{\partial}{\partial x_i}\left(\,V_i f\,\right) = -\frac{\partial}{\partial V_i}\left(\,a_i f\,\right) + \frac{\partial^2}{\partial V_i V_j}\left(\frac{1}{2}B_{ij} f\right)\ , \tag{2}$$

where $f = f(t; \mathbf{x}, \mathbf{V})$ is the (Lagrangian) PDF associated to the process $(\mathbf{X}_p(t), \mathbf{U}_p(t))$ and $\mathbf{B}$ the $\mathbf{b^t b}$ tensor. Therefore, adopting a Lagrangian point of view, with Eqs. (1), is helpful to develop a physics-based model as well as to provide a Monte Carlo solution of the Fokker-Planck equation (this is an example of the probabilistic interpretation of PDEs).

The coefficients $\mathbf{a}$ and $\mathbf{b}$, respectively known as the drift vector and the diffusion matrix, are to be determined. The matrix $\mathbf{b}$ is defined following Kolmogorov's similarity theory and the main closure issue is therefore the expression of the drift, *i.e.*, of the vector $\mathbf{a}$. First attempts were to assume a form for the PDF f solution of Eq. (2) that would provide conditions for the determination of $\mathbf{a}$. Along with that assumption, Thomson (1987) reviewed a set of criteria distinguishing 'good Lagrangian stochastic models from bad' and showed that these criteria were all lower or equivalent to the well-mixed criterion. However, the well-mixed criterion alone is not sufficient to define a unique model in three dimensions, and it was shown by Sawford and Guest (1988) and Borgas et al. (1997) that certain flow properties, besides the knowledge of f, need to be accounted for ('non-uniqueness within a class of models that are well-mixed within Thomson's criteria can not be resolved unless flow properties in addition to f are respected', see Wilson and Sawford (1996)). Historically, in the atmospheric literature, authors adopted other selection criteria and worked on a case-by-case basis (homogeneous or inhomogeneous turbulence, Gaussian or non-Gaussian turbulence hypothesis, convective, stable or neutral atmosphere, etc.). As a result, this confusion surrounding expressions of $\mathbf{a}$ has sometimes led to non well-mixed models that made various authors adopt a back-and-forth philosophy and add *ad-hoc* new drift terms to make up for the problem (see Lin and Gerbig (2013)).

Pope (1987)'s paper offered a whole new point of view, by setting the starting point on the mean Navier-Stokes and continuity equations. He showed that the fulfillment of the well-mixed criterion is independent from any model, as long as the mean pressure-gradient term, that is to say the non-modeled part of the Navier-Stokes momentum equation, is properly incorporated in the Langevin model. In other words, the well-mixed criterion is essentially the manifestation that the mean fluid velocity field derived from a Lagrangian model should be a zero-divergence field and satisfy the mean continuity and Navier-Stokes equations. Compared to other attempts, another valuable insight was to clarify the differences between Lagrangian and Eulerian PDFs, as well as their correspondence, and to show that Eulerian PDFs result from Lagrangian ones and are, therefore, outcomes of the modeling approach rather than inputs (see, in particular, a comprehensive account given in Pope (2000), chapter 12, while some definitions are recalled in Appendix B).

In the following subsections, the main points of this PDF approach are recalled and brought out by considering a very simple stochastic model that nevertheless contains the key notions for our general discussion.

2.2. The simplified Langevin model

The Generalized Langevin Model (GLM), developed by Pope (1985, 2000), writes:

$$dX_{p,i} = U_{p,i}\, dt \tag{3a}$$

$$dU_{p,i} = -\frac{1}{\rho_f}\frac{\partial \langle P_f \rangle}{\partial x_i} dt + G_{ij}(U_{p,j} - \langle U_{f,j} \rangle)\, dt + \sqrt{C_0 \epsilon_f}\, dW_i \ . \tag{3b}$$

In Eq. (3b), ρ_f is the fluid density and C_0 a constant given by Kolmogorov's theory, while $\langle U_{f,i} \rangle$, $\langle P_f \rangle$, k_f and ϵ_f are the mean velocity, pressure, turbulent kinetic energy and turbulent kinetic energy dissipation rate fields, respectively. The values of the fluid mean fields entering Eq. (3b) are to be understood as being the values taken at the particle location which means that, for example, $\langle U_{f,i} \rangle$ stands for $\langle U_{f,i} \rangle (t, \mathbf{X}_p(t))$. However, in the rest of the paper this explicit dependence is left out for the sake of keeping simple notations. The same is true for the matrix G_{ij} which expresses the return-to-equilibrium term and is modeled as a function of local values of fluid mean fields. A general expression consists in decomposing this matrix as follows

$$G_{ij} = -\left(\frac{1}{2} + \frac{3}{4} C_0\right) \frac{\epsilon_f}{k_f}\, \delta_{ij} + G^a_{ij} \ , \tag{4}$$

under the condition that Tr $(\mathbf{G}^a \mathbf{R}) = 0$, with $R_{ij} = \langle U'_{f,i}\, U'_{f,j} \rangle$ the Reynolds-stress tensor (with $U'_{f,i} = U_{f,i} - \langle U_{f,i} \rangle$ being the fluctuating component of the fluid velocity) to be consistent with the kinetic energy budget (cf. Pope (2000)).

Taking $G^a_{ij} = 0$ leads to the Simplified Langevin model (SLM), written here as:

$$dU_{p,i} = -\frac{1}{\rho_f}\frac{\partial \langle P_f \rangle}{\partial x_i}\, dt - \frac{U_{p,i} - \langle U_{f,i} \rangle}{T_L} dt + \sqrt{C_0 \epsilon_f}\, dW_i \ , \tag{5}$$

where T_L, which represents the Lagrangian integral timescale, is given by

$$T_L = \frac{1}{\frac{1}{2} + \frac{3}{4} C_0} \frac{k_f}{\epsilon_f} \ . \tag{6}$$

With respect to the general expression of a diffusion stochastic process in Eq. (1), the drift and diffusion coefficients for the SLM are easily identified:

$$a_i = -\frac{1}{\rho_f}\frac{\partial \langle P_f \rangle}{\partial x_i} - \frac{U_{p,i} - \langle U_{f,i} \rangle}{T_L} \ , \tag{7}$$

$$b_{ij} = \sqrt{C_0 \epsilon_f}\, \delta_{ij} \ , \tag{8}$$

which shows that the closure of the diffusion matrix is in line with Kolmogorov theory and the idea of statistically isotropic small-scales (here time scales) governed by the local value of the kinetic energy rate of dissipation.

Model written in terms of:	Formulation
Instantaneous velocity	$dU_{p,i} = -\frac{1}{\rho_f}\frac{\partial\langle P_f\rangle}{\partial x_i}\,dt\; -\frac{U'_{p,i}}{T_L}\,dt + \sqrt{C_0\epsilon_f}\,dW_i$
Fluctuating velocity	$dU'_{p,i} = \left(\frac{\partial\langle U'_{f,i}U'_{f,j}\rangle}{\partial x_j} - U'_{p,j}\frac{\partial\langle U_{f,i}\rangle}{\partial x_j}\right)dt\; -\frac{U'_{p,i}}{T_L}\,dt + \sqrt{C_0\epsilon_f}\,dW_i$

Table 1: Two possible formulations of the SLM.

It is important to realize that, in the formulations given above, the GLM is expressed in terms of the instantaneous fluid particle velocity $U_{p,i}$. However, most of the models used in the atmospheric literature are written in terms of the fluctuating velocity $U'_{p,i}$, defined as $U'_{p,i} = U_{p,i} - \langle U_{f,i}\rangle$. As such, there is no intrinsic difference between writing a Lagrangian stochastic model in terms of instantaneous or fluctuating velocities since this amounts to a simple change of variables to go from one formulation to the other. These equivalent formulations of a Lagrangian stochastic model have already been discussed in the literature, for instance in Minier and Peirano (2001), section 7.5.2. They were recently analyzed, among other possible alternative formulations, in Minier et al. (2014) using a general expression of Lagrangian stochastic models to emphasize that the issue of the well-mixed condition (also referred to as the 'spurious-drift effect') is not related to the specific form of a model for the fluctuating part of the drift vector as well as for the diffusion matrix but, simply, to the proper account of the mean pressure-gradient term.

The derivation of the formulation of a Lagrangian stochastic model in terms of fluctuating particle velocities is recalled in Appendix A and readers are also referred to the above-mentioned works for detailed analysis. However, for the sake of clarity and to illustrate this general framework, we have chosen to present key results with the simplest class of Lagrangian stochastic models, represented here by the SLM.

The two types of formulation for the SLM are summarized in Table 1. The common part to both formulations, displayed in blue, includes the specific details of the chosen stochastic model (in the present case, the basic form of a Langevin model). What is relevant for our discussion is expressed by the terms, displayed in black, on the rhs (right-hand side) of both equations. In the formulation written with instantaneous velocities, the mean pressure gradient appears directly in the model, as it should for the mean particle acceleration conditioned at a given location to be consistent with the mean Navier-Stokes equation (leaving out the mean viscous term for high Reynolds-number flows). This is not the case in the formulation written in terms of fluctuating velocities, where it is expressed through the term between brackets $(\partial\langle U'_{f,i}U'_{f,j}\rangle/\partial x_j - U'_{p,j}\partial\langle U_{f,i}\rangle/\partial x_j)dt$ which also includes convective transport in non-homogeneous flows. This can be further brought out by considering mean

particle accelerations (or, rather, conditional mean velocity increments) conditioned on a given location, which are

$$\langle dU_{p,i} \,|\, \mathbf{X}_p(t) = \mathbf{x} \rangle = -\frac{1}{\rho_f} \frac{\partial \langle P_f \rangle}{\partial x_i} \, dt \ , \tag{9}$$

$$\langle dU'_{p,i} \,|\, \mathbf{X}_p(t) = \mathbf{x} \rangle = \frac{\partial \langle U'_{f,i} U'_{f,j} \rangle}{\partial x_j} \, dt \ . \tag{10}$$

Note that these equations are obtained by writing that $\langle \mathbf{U}'_p \rangle = 0$, which is actually another form of the well-mixed condition and a translation of the fact that there is no spurious-drift effect. These expressions demonstrate that forgetting to include the derivative term of the Reynolds-stress tensor (cf. the rhs of Eq. (10)) is equivalent to forgetting the mean-pressure-gradient term in the resulting mean Navier-Stokes equation. In numerical applications, this is reflected by particles being driven away from high energy-content regions and accumulating in low energy-content ones or, in other terms, by spurious drifts.

The second term appearing on the rhs of the formulation in terms of fluctuating velocities, $-U'_{p,j} \, \partial \langle U_{f,i} \rangle / \partial x_j$, does not contribute directly to mean drift effect and, therefore, does not play a role for the well-mixed condition. It is however essential to retrieve the correct production terms in the corresponding transport equations for the Reynolds-stress tensor, *i.e.*, the so-called $R_{ij} - \epsilon$ equations. Along with the well-mixed condition, this point is discussed at length in Minier et al. (2014).

Although both expressions are equivalent, it appears from the requirements to retain all the terms appearing on the rhs of the form written in terms of fluctuating components that this formulation has very little practical interest. Indeed, the model written for instantaneous velocities is more tractable since it requires only three gradients (for $\langle P_f \rangle$) compared to the 18 needed in the fluctuating-velocity formulation (9 for $\partial \langle U_{f,i} \rangle / \partial x_j$ and 9 for $\partial \langle U'_{f,i} U'_{f,j} \rangle / \partial x_j$). This explains that, apart for theoretical developments and the analysis of consistency issues between turbulence models (to be discussed in section 2.3), it is both safer and easier to implement models in terms of instantaneous velocities (see discussions in Minier et al. (2014)).

2.3. On turbulence model consistency issues in hybrid Eulerian/Lagrangian methods

If the proper introduction of the mean pressure gradient on the rhs of Eq. (3) is enough to ensure that the mean Navier-Stokes equation derived from the PDF model is correctly retrieved, the specific details of a Langevin model (*i.e.*, the last two terms on the rhs of Eq. (3b)) come into play when considering the second-order velocity moments or, in other words, the transport equations for the Reynolds-stress components. The connection between Lagrangian stochastic models was first developed in Pope (1994b) and has been addressed in details in several works, cf. Pope (2000); Minier and Peirano (2001); Minier et al. (2014). For the sake of completeness, the main steps and results are recalled in Appendix B and are simply referred to in this section.

The derivation of the Reynolds-stress equations from a Langevin model, such as the GLM in Eqs. (3), reveals that for each formulation of a Langevin model there is a corresponding second-order, or $R_{ij} - \epsilon$, turbulence model. This connection is of importance, first to indicate that Lagrangian stochastic are true second-order turbulence model when they are used as stand-alone approaches and, second, to point out a consistency issue when they are used in hybrid Eulerian/Lagrangian numerical formulations.

In hybrid Eulerian/Lagrangian calculations, a classical CFD (Computational Fluid Dynamics) code is first run to obtain fields made up by mean fluid variables, *e.g.*, $\langle U_{f,i} \rangle(t, \mathbf{x})$, $\langle U'_{f,i}\, U'_{f,j} \rangle(t, \mathbf{x})$, $\epsilon_f(t, \mathbf{x})$, etc. The name Eulerian refers to the field-based approach usually followed in CFD codes, where fields are obtained as solutions of PDEs through traditional numerical techniques on a mesh discretization. These fields are then provided to the particle-based, or Lagrangian, formulation where they are used in the SDEs to simulate particle dynamics. For example, the value of the mean fluid velocity at particle location that enters the return-to-equilibrium term in the GLM, cf. the second term on the rhs of Eq. (3b), is obtained by interpolating the mean fluid velocity field provided by the Eulerian simulation and is used to advance instantaneous particle velocities.

Compared to stand-alone approaches, one interest of this hybrid formulation is to handle mean fields that are free of statistical noise. This raises, however, a consistency issue since some fluid variables are simulated both by the Eulerian and Lagrangian solvers. For example, the fluid mean velocity field is obtained from the mean Navier-Stokes equation solved in the Eulerian solver with a turbulence model and also from the Lagrangian one by Monte Carlo estimations derived from the set of instantaneous particle velocities. Note that, depending on the details of the hybrid method, the same is true for the second-order moment R_{ij}, or its trace the fluid turbulent kinetic energy k_f. This means that there is, for some moments, a double prediction and these fields are therefore called 'duplicate fields'. However, since they correspond to the same physical variable, it is essential to ensure that both predictions yield the same result. This is referred to as the consistency issue.

As mentioned above, Lagrangian stochastic models correspond to second-order turbulence models. Consequently, if a GLM is retained as the particle stochastic model, a consistency formulation consists in using a second-order model with the same model for the pressure-rate-of-strain closure in the Eulerian solver. This is recalled in Appendix B for the GLM. In particular, if a SLM is chosen to describe particle velocity evolution in the Lagrangian solver, then this implies that a Rotta second-order turbulence model should be used in the Eulerian one (with the Rotta constant deriving from the value taken from the C_0 constant, cf. Appendix B).

In practical simulations, the consistency issue needs to be assessed, especially when inconsistent formulations are retained. This is the case when, for instance, a $k-\epsilon$ model is used as the turbulence model in the Eulerian solver while a GLM is used in the Lagrangian one. Indeed, there is an intrinsic difference between eddy-viscosity closures and particle-based methods where particle velocity is explicitly tracked (see a comprehensive discussion in sections 10.3 and 10.4 of Minier (2016)) and the impact of such inconsistent hybrid

formulations has to be carefully evaluated. To the authors' knowledge, few studies have addressed this issue (see Chibbaro and Minier (2011); Minier (2015)), which still needs to be emphasized and whose importance has to be monitored. This is done in section 5.

2.4. Wall-boundary conditions treatment

Another issue is the formulation of wall-boundary conditions in particle stochastic approaches, which is a subject that has received little attention. For instance, a first idea consists in applying specular rebound: every particle that crosses a wall boundary and exits the computational domain is reflected back with the same longitudinal velocity as the incoming one. Yet, this amounts to writing a zero-flux boundary condition for the longitudinal velocity component, which fails to account for the momentum exchange with the wall. Following the same spirit of the one used to derive so-called wall-function boundary conditions in CFD codes, where a boundary condition is applied in the logarithmic region near the wall rather than at the wall itself (cf. Pope (2000)), a better representation of wall-boundary conditions to capture the constant-stress boundary layer is (assuming that z is the wall-normal direction):

$$U_{p,x}^{in} = U_{p,x}^{out} - 2\frac{\langle U'_{f,x}U'_{f,z}\rangle}{\langle U'^2_{f,z}\rangle}U_{p,z}^{out} \ , \tag{11a}$$

$$U_{p,y}^{in} = U_{p,x}^{out} - 2\frac{\langle U'_{f,y}U'_{f,z}\rangle}{\langle U'^2_{f,z}\rangle}U_{p,z}^{out} \ , \tag{11b}$$

$$U_{p,z}^{in} = -U_{p,z}^{out} \ , \tag{11c}$$

where the subscript 'in' stands for the particle's incoming velocity value and 'out' the outgoing one (see Fig. 1). The rationale behind these expressions for particle-based stochastic models are detailed in Dreeben and Pope (1997); Minier and Pozorski (1999).

Such formulations are needed to reproduce the correct behavior of the mean longitudinal fluid velocity in wall boundary layers. In hybrid Eulerian/Lagrangian approaches, they represent also an additional consistency issue since wall-boundary conditions are actually formulated twice, in the Eulerian and in the Lagrangian solvers. In section 5, we will see that consistent wall-boundary conditions are important for the correct computation of particle second-order moments near walls.

3. Numerical assessment of the well-mixed criterion

In this section, we illustrate the points addressed in section 2 with numerical applications. To this end, three cases are studied:

- a mixing layer (free shear-flow);
- an infinite channel flow (simple wall-bounded flow);
- a flow around an obstacle in a neutral boundary layer (complex wall-bounded flow).

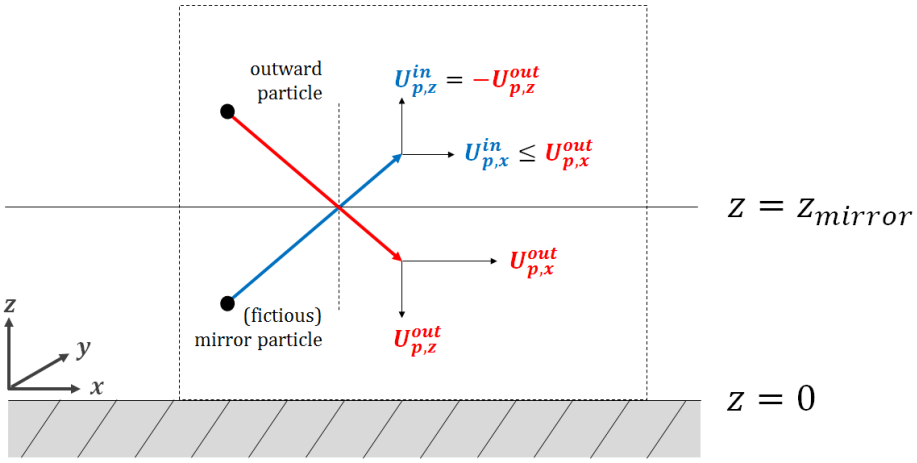

Figure 1: Sketch of the wall/particle interaction showing how particles arriving at $z = z_{mirror}$, which is chosen in the logarithmic layer, are reflected back in the domain so as to respect a zero-mass flux in the wall-normal direction as well as the momentum exchange due to friction in the longitudinal one. $\mathbf{U}_p^{in}$ (oriented upward) and $\mathbf{U}_p^{out}$ (oriented downward) stand for the inward and outward velocities, respectively.

These three cases allow to test theoretical and numerical formulations in situations where different effects come into play. The mixing layer case is a non-homogeneous turbulent flow, with a laminar/turbulent transition at the edges of the mixing layer but without flow reversal or wall effects. On the other hand, the infinite channel flow is a simple one-dimensional but non-homogeneous flow, essentially driven by the wall-boundary conditions. Finally, the case of the flow around an obstacle located on a wall in a neutral atmospheric boundary layer gathers all difficulties: it is a non-homogeneous turbulent flow, involving wall effects and complex flow recirculation patterns that make it a stringest test case to assess the respect of the well-mixed criterion and consistency requirements.

In order to concentrate on the issues raised in section 2 and avoid additional ones related to the implementation of elaborate turbulence models, it was chosen to retain the simplest possible consistent formulation. For this reason, a second-order Rotta model was selected in the Eulerian simulations while the SLM was used for the Lagrangian ones.

The calculations were performed using the open-source CFD code *Code_Saturne* (cf. `http://code-saturne.org/`), developed at EDF R&D. Details on the numerical methods implemented in the code can be found in Archambeau et al. (2004) for the Eulerian solver and in Peirano et al. (2006) for the Lagrangian one. It can be noted that the Lagrangian module is a general one developed for discrete, or non-zero inertia, particles but that fluid particles (or tracer-particle limit) are simply simulated by putting the particle relaxation timescale to zero (this is correctly handled numerically by considering exponential numerical schemes, as detailed in Peirano et al. (2006)).

Since present cases correspond to steady-state flows, hybrid Eulerian/Lagrangian simulations are performed sequentially:

- first, the Eulerian solver is run and, at convergence, calculations are stopped and

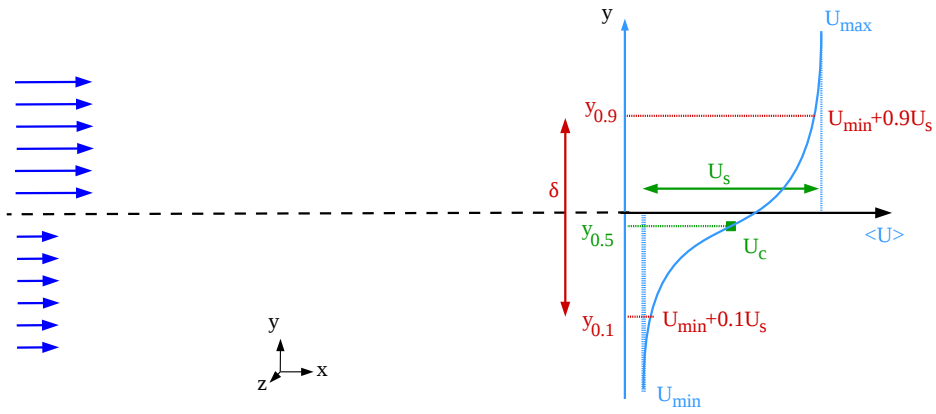

Figure 2: Sketch of a plane 2D mixing layer showing the characteristic convective velocity U_c, velocity difference U_s, width of the flow $\delta(x)$ and key lateral positions.

the mean velocity, pressure and turbulence fields are frozen. These simulations are obtained with the second-order Rotta turbulence model (with $C_R = 4.15$);

- second, particles are introduced and tracked within the pre-calculated flow fields. The SLM is retained to model fluid particle velocity evolutions (with $C_0 = 2.1$).

3.1. The mixing layer case

3.1.1. Case description and fluid phase simulation

Mixing layers correspond to turbulent flows formed between two uniform, nearly parallel streams of different velocities U_{max} and U_{min}. Fig. 2 displays the typical sketch of a mixing layer created by the interaction between two streams with different velocities. In the present case, the dominant direction of flow is x, the cross-stream coordinate is y and statistics are independent of the spanwise coordinate, z. The mean velocity can thus be written $\langle \mathbf{U}_f(x,y,z) \rangle = \langle \mathbf{U}_f(x,y) \rangle$. Numerous studies have shown that the flow is self-similar and depends on some characteristic parameters (more details can be found in Pope (2000); Champagne et al. (1976)):

- the characteristic convection velocity

$$U_c = \frac{1}{2}\left(U_{max} + U_{min}\right) \ , \tag{12}$$

- the characteristic velocity difference

$$U_s = \left(U_{max} - U_{min}\right) \ , \tag{13}$$

- the characteristic width of the flow

$$\delta(x) = y_{0.9}(x) - y_{0.1}(x) \ , \tag{14}$$

  defined here as the extent of the region where the fluid velocity ranges from $U_{min} + 0.1U_s$ to $U_{min} + 0.9U_s$ (see Figure 2).

- the characteristic reference lateral position

$$\overline{y}(x) = \frac{1}{2}\left(y_{0.9}(x) + y_{0.1}(x)\right) \ . \tag{15}$$

These characteristic values allow to define a scaled velocity

$$f(\xi) = \frac{\langle U \rangle - U_c}{U_s} \ , \tag{16}$$

which depends only on the scaled cross-stream location (self-similar flow)

$$\xi = \frac{y - \overline{y}(x)}{\delta(x)} \ . \tag{17}$$

Similarly, the Reynolds stresses have been shown to be self-similar when scaled by U_s^2. Experimental data have also shown that the spreading parameter S defined as

$$S = \frac{U_c}{U_s}\frac{d\delta}{dx} \tag{18}$$

is independent of the velocity ratio and thus constant. Reported values are in the range $S = 0.06$ to $S = 0.11$.

The test case considered consists in a flow within a rectangular domain, whose dimensions are $10\ m \times 0.8\ m \times 0.004\ m$, with two different inlet velocities. The grid comprises 10 000 rectangular uniform cells and boundary conditions are as follows.

Inlet boundary. The flow is divided in two regions each with a uniform velocity profile: $U = 2.0\ m.s^{-1}$ for $y < 0.4\ m$ and $U = 3.0\ m.s^{-1}$ for $y > 0.4\ m$. Thus, $U_{min} = 2\ m.s^{-1}$ and $U_s = 1\ m.s^{-1}$.

Upper and lower boundaries. Symmetry (zero-flux) condition.

First, we assess numerical results obtained for the fluid phase simulation with respect to existing experimental data (more details on experimental results for such free shear-flows can be found in Pope (2000); Champagne et al. (1976)). The mean velocity field inside the domain is displayed in Fig. 3 where it can be seen that the mixing of the two initial laminar streams having different inlet velocities leads to the growth of a turbulent region along the longitudinal direction with a continuous range of mean fluid velocities.

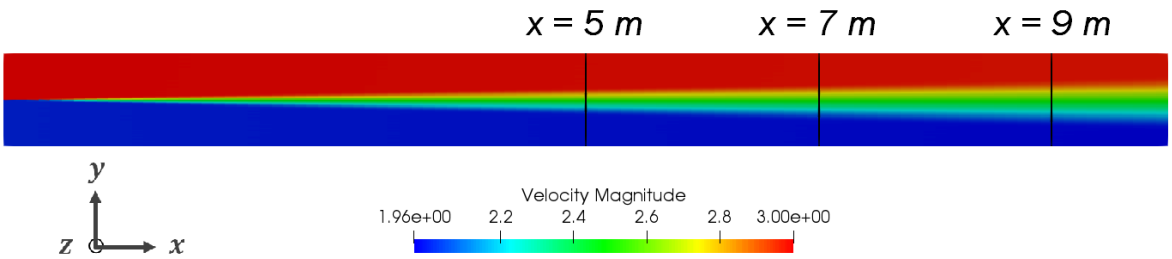

Figure 3: Snapshot of the longitudinal mean fluid velocity obtained from the Eulerian simulation showing the formation and growth of a turbulent mixing layer (the three vertical lines are used to extract data to assess self-similarity and analyze results).

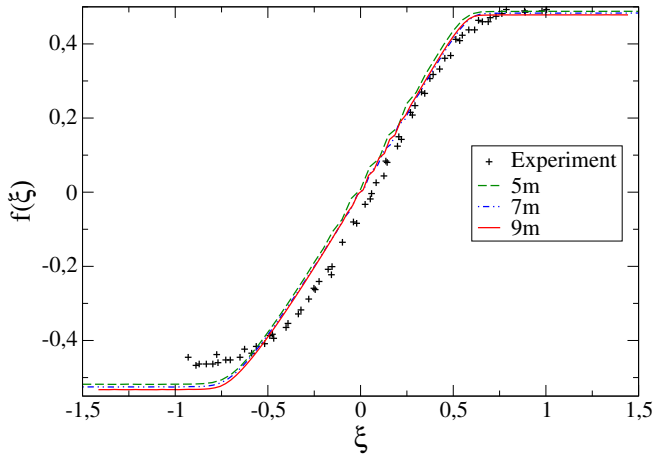

Figure 4: Profile of the scaled mean longitudinal velocity across the mixing layer: comparison between experimental data (symbols) and numerical results sampled at various distances from the inlet (lines).

To further characterize the predicted mean fluid flow, profiles are taken along three vertical lines located at three different positions downstream of the splitter plate (they correspond to the three vertical lines drawn at $x = 5\,m$, $x = 7\,m$ and $x = 9\,m$ in Fig. 3). The scaled longitudinal mean velocity profile is displayed in Fig. 4. It can be seen that numerical results are in good agreement with experimental data and that self-similarity is also well captured by the numerical simulations.

This is further confirmed by considering the scaled Reynolds stresses, which are plotted in Fig. 5. It is seen that self-similarity is also achieved and that results are in line with experimental values, even though some discrepancies can be observed. For example, R_{33} reproduces the experimental profile but underestimates the maximum value (a 40% error is made). At this stage, it is worth recalling that a simple $R_{ij} - \epsilon$ model (*i.e.*, the Rotta model) was used whereas it is known that more developed second-order models, accounting explicitly for mean velocity gradients such as the ones occurring in mixing layers, yield much-improved predictions (see detailed discussions in Pope (2000)). However, it should also be recalled that the present objective is to assess the respect of the well-mixed condition

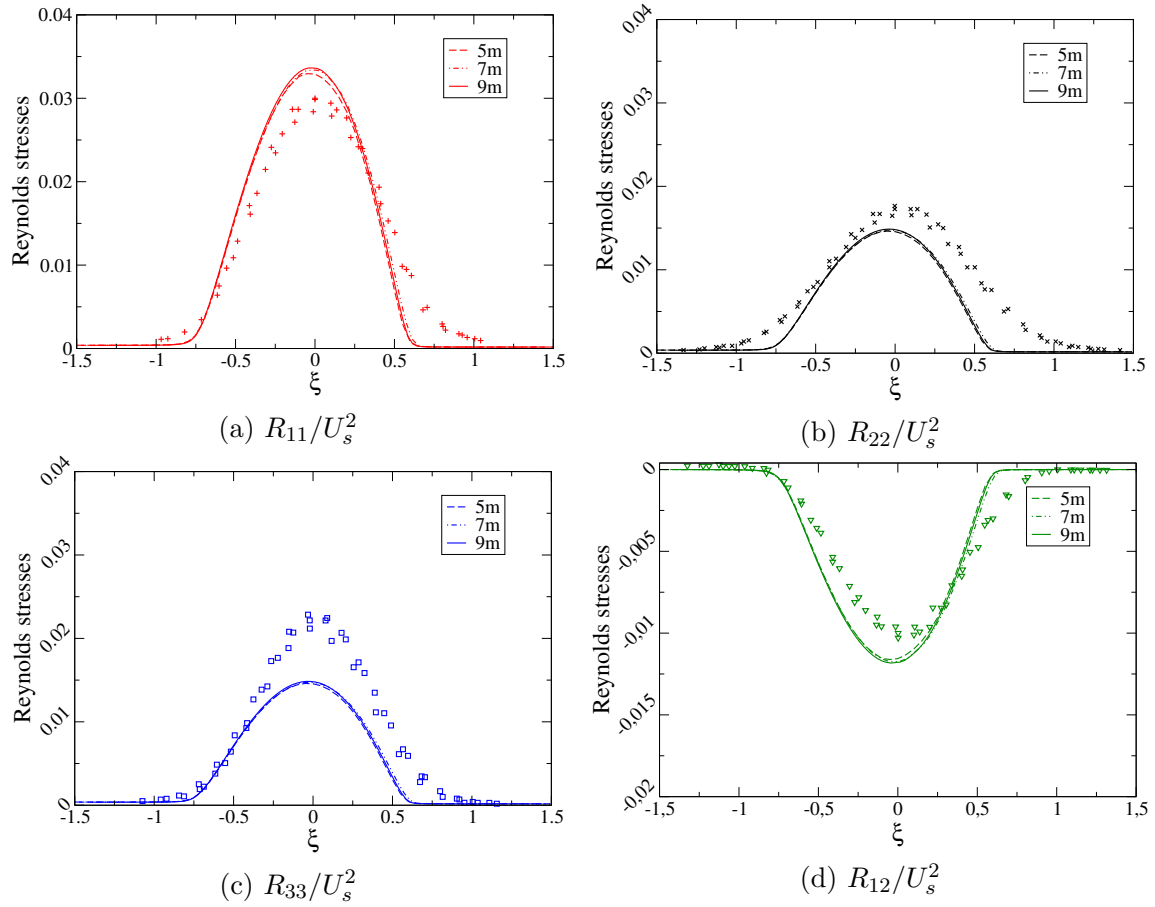

Figure 5: Profiles of the scaled Reynolds stresses across the mixing layer: comparison between experimental data (symbols) and numerical results sampled at various distances from the inlet (lines).

and of consistency requirements. In that sense, this paper is not about the ability of given $R_{ij} - \epsilon$ turbulence models to reproduce perfectly experimental values (they are given here merely as a reference) but is about assessing whether fluid particle concentration remains uniform and whether moments of the velocity field predicted by the Eulerian and Lagrangian simulations are consistent. Particle concentration results obtained from the particle phase simulation are now discussed while consistency is addressed in section 5.

3.1.2. Results for particle concentration

In the mixing layer case, simulations were run with a domain initially void of fluid particles which are then injected until a steady-state regime is reached, where a statistically-constant number of particles are present within the computational domain (*i.e.*, when, on average, the same number of particles are leaving the domain through the exit plane as the ones injected through the inlet section). In the numerical simulations, each fluid particle represents an equal amount of fluid mass and, consequently, the number of particles being injected through the two inlet sub-sections corresponding to the two different streams must

be so that the inlet mass flow rates are respected. Then, given the velocities imposed at the inlet for the two streams (2 $m.s^{-1}$ for $y < 0.4\ m$ and 3 $m.s^{-1}$ for $y > 0.4\ m$), it was chosen to inject 80 particles during each time step through the low-speed stream inlet (for $y < 0.4\ m$), which means that 120 particles were injected through the high-speed stream one (for $y > 0.4\ m$). When a steady-state was reached, the domain contained a number of particles of the order of $N = 80\,000$, *i.e.*, about 8 particles per cell. Therefore, in the steady-state regime, Monte Carlo estimates were also averaged over time (over 2 000 time steps), using an ergodic assumption, in order to reduce statistical noise to low levels. This means that, on average, 16 000 particles per cell were used to obtain statistics.

Since the objective of the simulation is to assess whether the well-mixed criterion is respected, we consider the normalized particle concentration and check that it remains constant in the simulation domain (particles should not accumulate in specific regions or be depleted from others). The actual particle number density obtained in the computations depends on the chosen numerical parameters, that is essentially the number of fluid particles injected during each time step and the mesh size (each cell having the same volume), but is not of significance provided it is high enough for statistics to be statistically relevant. What is relevant is the normalized particle number, or particle concentration, obtained by dividing the actual number of particles in any cell by the mean one.

Numerical results for this normalized particle concentration are shown in Fig. 6. In Fig. 6a, the horizontal concentration profile taken at mid height ($y = 0.4\ m$), that is at the same height as the splitter plate, is plotted. A depletion zone can be seen near the inlet (roughly between the inlet and $x = 1\,m$, whose value depends on the choice of initial velocities and mesh sizes) that corresponds to the distance needed for the particles to correctly mix in the domain. Indeed, in the first simulations, the initial particle distribution across the inlet section was clumpy with, in each inlet cell, sub-groups of particles being injected at the center of each inlet elementary surface rather than being also uniformly distributed across elementary inlet surfaces. This was later corrected in the code but it was nevertheless decided to present, for the mixing layer case, the results obtained with this clumpy injection since it provides an additional test to check whether a properly-formulated Lagrangian stochastic model can mix particles and drive the distribution of particle positions from a clumpy one (a sum of Dirac-functions) to a continuous and uniformly-distributed one.

From the profile in Fig. 6a, it is seen that particles are indeed correctly driven to a well-mixed state and that, once achieved, a uniform concentration is maintained in the rest of the domain. This is further confirmed by plotting the vertical profiles at the sections $x = 7$ and $9\ m$, see Fig. 6b, which reveal that a uniform particle concentration is obtained throughout the domain. In other words, the well-mixed criterion is satisfied in the mixing layer case, which is representative of non-homogenous turbulent free shear-flows.

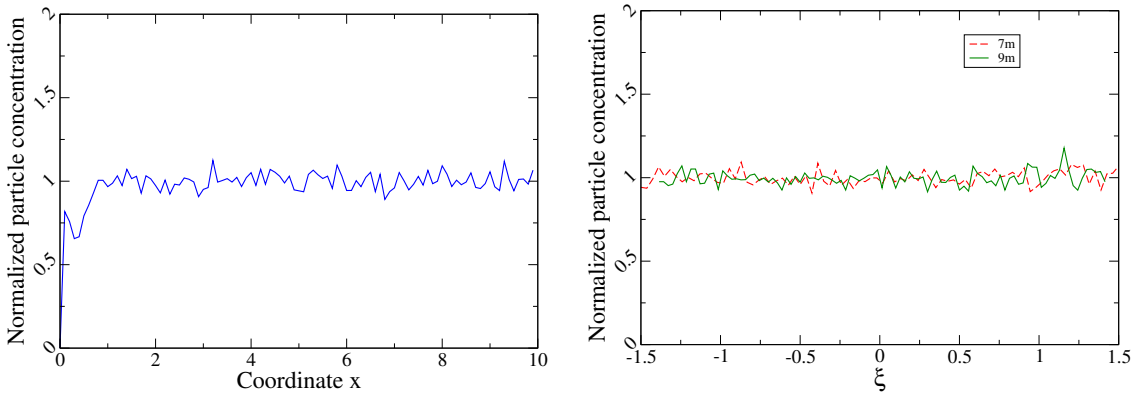

(a) Horizontal profile ($y = 0.4\ m$)

(b) Vertical profiles

Figure 6: Profiles of the particle normalized concentration in the plane mixing layer: (a) sampled longitudinally along the middle of the layer; (b) sampled vertically at various distances from the inlet.

3.2. The infinite channel flow

3.2.1. Case description and fluid phase simulation

The second test case corresponds to an infinite half-channel flow, which is represented as a vertical column of 20 cells of dimensions $0.05\ m \times 0.05\ m \times 0.05\ m$. Since this is basically a one-dimensional flow where statistics depend only on the wall-normal coordinate, the flow is simply generated by applying a periodicity condition between the upstream and downstream faces (see Fig. 7) and by imposing in the longitudinal direction a momentum source term that corresponds to the mean pressure gradient (or pressure loss) $d\langle P_f \rangle / dx = -\rho_f u_*^2 / H$, where $\rho_f = 1.18\ kg.m^{-3}$ is the density of air, $H = 1\ m$ the half-height of the channel, and $u_* = 0.05\ m.s^{-1}$ the chosen value of the friction velocity at the wall.

Once a steady state is obtained, the profiles of the mean longitudinal velocity and of the non-zero velocity second-order moments are expressed in terms of the relevant wall units, *i.e.*, $u_*\,(m/s)$ and $\nu/u_*\,(m)$ where $\nu = 1.55 \times 10^{-5}\ m^2.s^{-1}$ is the air kinematic viscosity. The resulting profiles of the scaled mean velocity U/u_* and the scaled Reynolds stresses R_{ij}/u_*^2 are given in Fig. 8, as a function of the normalized wall-normal distance $z^+ = zu_*/\nu$. These results are fairly classical for a Rotta turbulence model in a turbulent boundary layer with a wall-function approach, which means that only the so-called logarithmic layer is simulated and that the boundary condition is met to bridge over the viscous-layer to avoid a computationally-demanding down-to-the-wall numerical integration with a velocity no-slip condition at the wall (see Minier and Pozorski (1999); Pope (2000)). As for the mixing-layer case, the objective is not to obtain the best possible numerical results for fluid profiles but rather to use representative results to check whether particle concentration profiles are correctly captured. It is worth noting that wall-boundary conditions play a key role in the infinite channel flow and, therefore, this case is a test for a non-homogeneous situation (in the wall-normal direction) but also for the application of relevant particle boundary conditions as discussed in section 2.4.

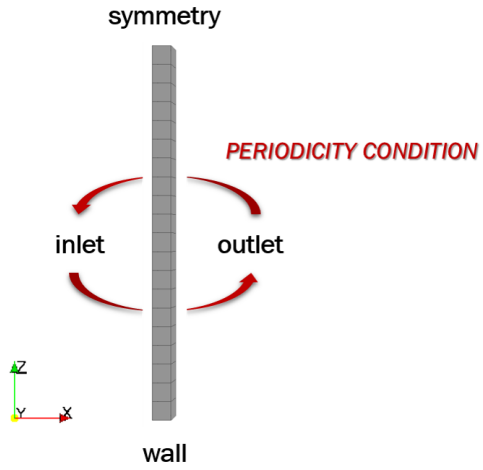

Figure 7: Sketch of the computational domain for the infinite plane channel simulation.

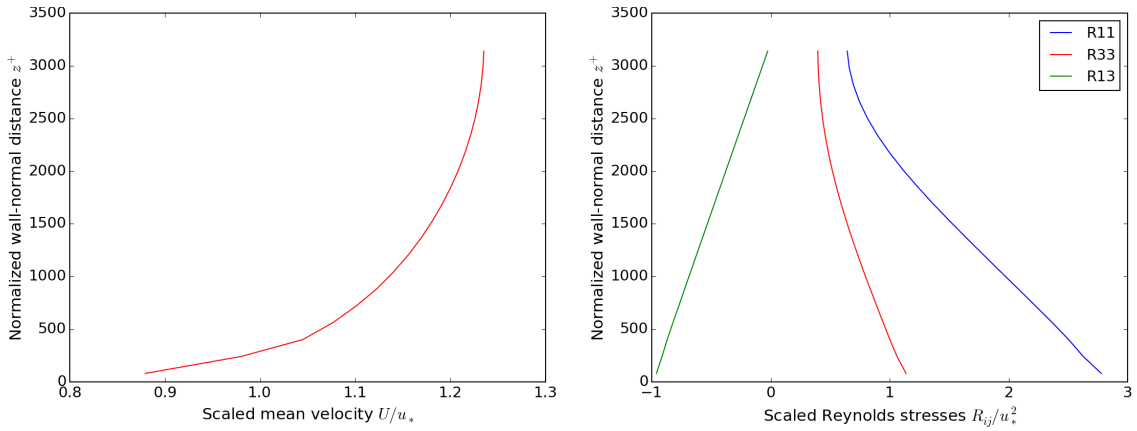

(a) Scaled mean fluid velocity

(b) Scaled Reynolds stresses

Figure 8: Vertical profiles of the scaled mean velocity (a) and Reynolds stresses (b) as a function of the normalized wall-normal distance $z^+ = zu_*/\nu$ for the infinite plane channel case.

3.2.2. Results for particle concentration

Then, $N = 200\,000$ particles uniformly distributed over the domain are injected and are tracked during a time lapse long enough for one particle to be transported by turbulent diffusion several times over the length of the half-channel flow so that results truly reflect the governing stochastic model rather than the memory of the initial conditions. The purpose is to check that a steady state is reached, where particle concentration remains uniform across the whole channel. As in the mixing layer case, the actual mean concentration, which depends on numerical parameters (the number of particles and the height of each cell), is of no direct significance and we only consider normalized concentrations. In this case, there is neither inlet nor outlet of particles and the average number of particles in a cell is around 10 000, that is high-enough for statistics to be obtained directly through Monte Carlo estimations without using any time-averaging. Incidentally, this allows to test another way to derive statistics and to assess whether they remain stationary in time.

Fig. 9 shows a scatter plot of particle positions in the domain at the end of the calculation, along with the corresponding concentration vertical profile derived from it. It can be seen that the concentration is constant over the whole height of the channel, indicating that a truly uniform particle distribution is obtained. For a more quantitative analysis, the vertical profiles of the normalized concentration $c/\langle c\rangle$ derived at different time steps in the calculation are displayed in Fig. 10a to check that uniformity across the channel is maintained in time.

It can be seen that the normalized concentration profiles oscillate with some noise around 1 and it is interesting to analyze the nature of these fluctuations. For that purpose, we consider the global spatial error defined as:

$$\frac{\sigma_c}{\langle c\rangle} = \frac{1}{\langle c\rangle}\sqrt{\frac{\sum_{j=1}^{N_{cells}}(c(\mathbf{x}_j) - \langle c\rangle)^2}{N_{cells}}} \tag{19}$$

where $N_{cells} = 20$ is the number of cells and $\mathbf{x}_j$ denotes the position of the center of the computational cells. Particle concentration is uniform in the domain if and only if the global spatial error $\sigma_c/\langle c\rangle$ equals zero. In the present case, it is found to be 0.626% at the end of the calculation. However, we are dealing with Monte Carlo estimates and statistical error needs to be accounted for. This error writes (see the derivation in Appendix C):

$$\left(\frac{\sigma_c}{\langle c\rangle}\right)_{Monte\ Carlo} = \sqrt{\frac{N_{cells}}{N}} \tag{20}$$

where N is the number of particles in the domain. With present values, this Monte Carlo error is therefore equal to 1%. Finally, the local error in each cell (defined as: $(c - \langle c\rangle)/\langle c\rangle$) is found to remain within -1.48% and 0.074%, which confirms that a uniform particle distribution is achieved across the height of the channel.

On the other hand, when the mean pressure-gradient term is removed from the Langevin model, particles tend to accumulate at the top of the domain, as revealed by the normalized

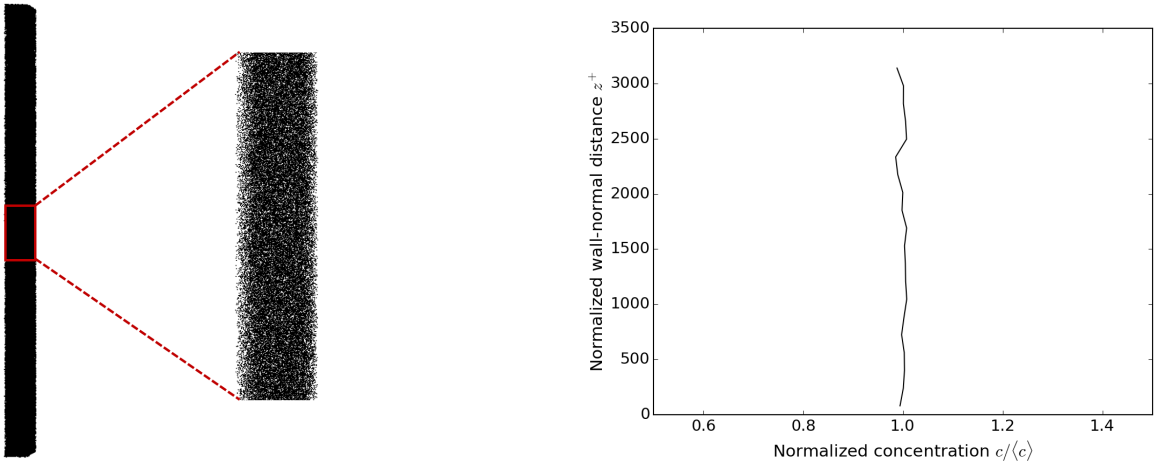

Figure 9: Particle repartition at the end of the calculation (left side) and the corresponding profile of the particle concentration (right side), showing the respect of the well-mixed criterion.

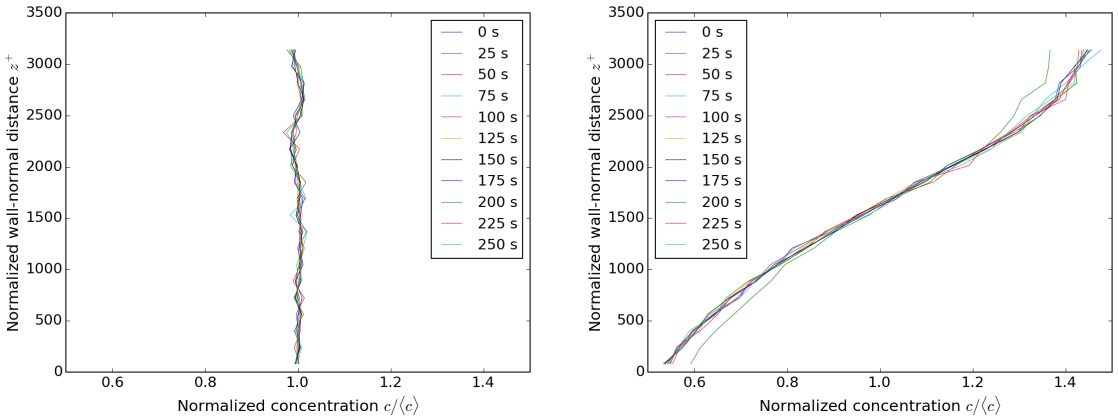

(a) With the mean pressure-gradient term (b) Without the mean pressure-gradient term

Figure 10: Vertical profiles of the normalized particle concentration at different time steps: (a) with the mean pressure-gradient term; (b) without it.

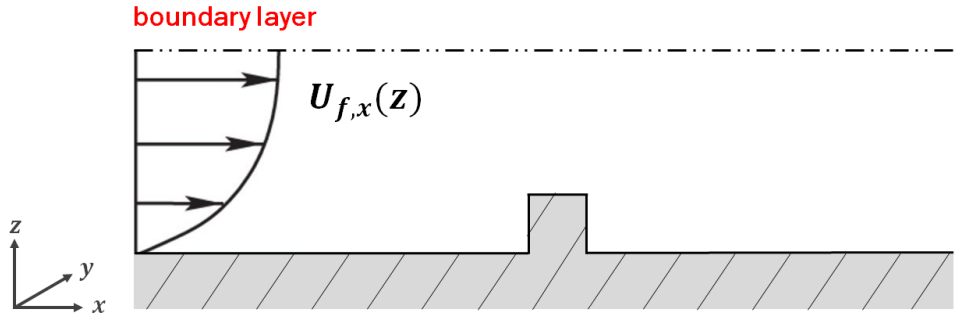

Figure 11: Sketch of a 2D flow around an obstacle within a boundary layer, where $U_{f,x}(z)$ is the imposed inlet velocity.

concentration profiles shown in Fig. 10b. In the case of the infinite channel flow, it is easy to understand why, in the absence of the mean pressure-gradient term, particle are driven towards low-energy zones. Indeed, the classical expression of the mean-momentum balance equation in the wall-normal direction gives that

$$\frac{1}{\rho_f}\frac{d\langle P_f\rangle}{dz} + \frac{dR_{33}}{dz} = 0 \ , \tag{21}$$

showing that removing the pressure-gradient term is equivalent to a spurious particle driving force along the direction of dR_{33}/dz. In that case, significant errors, reaching values up to 30.8%, are introduced, indicating that the general formulation without the mean pressure gradient is deeply flawed.

3.3. Obstacle within a neutral boundary layer

3.3.1. Case description and fluid phase simulation

The third test case studied in this work corresponds to a flow around a square obstacle placed on the bottom wall inside a neutral boundary layer. The spanwise dimension of the square obstacle is large enough to be regarded as infinite with respect to other characteristic lengths and the mean flow is therefore a 2D flow in the plane made up by the longitudinal and wall-normal directions. The geometry is sketched in Fig. 11 and the whole domain has the size of a $5\ m \times 0.1\ m \times 1\ m$ box. This test case is thus representative of situations usually addressed in atmospheric dispersion studies.

For that reason, inlet conditions are chosen so as to reproduce flow features typical of a rough boundary layer, as detailed in Table 2. Strictly speaking, these inlet conditions do not play a significant role as the flow develops itself downstream of the injection and reproduces the characteristics features of a channel flow before reaching the obstacle, where complex flow patterns are created. They are nevertheless applied to simulate typical boundary conditions. Note that with present dimensions, mean longitudinal velocities range from a near-zero value close to the wall to about $10\,m.s^{-1}$ at the upper boundary plane.

Field	Value or expression
$\langle U_{f,x} \rangle$	$\frac{u_*}{\kappa} \log\left(\frac{z+z_0}{z_0}\right)$
$\langle U_{f,y} \rangle$	$0\ m.s^{-1}$
$\langle U_{f,z} \rangle$	$0\ m.s^{-1}$
u_*	$0.5\ m.s^{-1}$
k	$u_*^2/\sqrt{C_\mu}$, $C_\mu = 0.09$
ϵ_f	$(u_*)^3/(\kappa(z+z_0))$ $\kappa = 0.42$, $z_0 = 0.0025\ m$
$\langle U'^2_{f,x} \rangle$	$(2/3)k$
$\langle U'^2_{f,y} \rangle$	$(2/3)k$
$\langle U'^2_{f,z} \rangle$	$(2/3)k$
$\langle U'_{f,x} U'_{f,y} \rangle$	$0\ m^2.s^{-2}$
$\langle U'_{f,x} U'_{f,z} \rangle$	$-u_*^2$
$\langle U'_{f,y} U'_{f,z} \rangle$	$0\ m^2.s^{-2}$

Table 2: Inlet dynamical fields for the case of the obstacle within a boundary layer.

A simple mesh made up by 798 400 cubic cells is used and the Eulerian simulation is run until a statistically steady-state is reached at convergence. The complex flow structure created by the obstacle is first revealed by showing isovalues of the velocity magnitude and kinetic energy (obtained as half the trace of the Reynolds stress tensor), as done in Fig. 12. It is seen that a strongly non-homogeneous flow is induced by the impact of the incoming stream on the obstacle, with high levels of kinetic energy in the high-shear region appearing downstream of the obstacle and separating the main longitudinal stream from the recirculation zone behind the obstacle. With present dimensions and flow velocities, a complex flow pattern is observed, as brought out by plotting the mean velocity field in Fig. 13. This figure indicates that a large recirculation zone is formed downstream of the obstacle but a zoom of the region just above the obstacle (see the lower part in Fig. 13) indicates that another recirculation is created between the top wall of the obstacle and the main stream flowing above. This represents indeed a very complex flow structure, involving wall effects, recirculating and high-shear regions.

Furthermore, isovalues of the Lagrangian timescale T_L, shown at the bottom of Fig. 12 reveal that widely different values, covering three orders of magnitude, are observed. This represents a challenging situation for the simulation of particle dynamics and, consequently, a severe test to assess the respect of the well-mixed criterion.

3.3.2. Particle phase simulation

In order to test different initialization procedures, particle simulations were not run starting from a initially void-of-particle domain as for the mixing layer case but by initial-

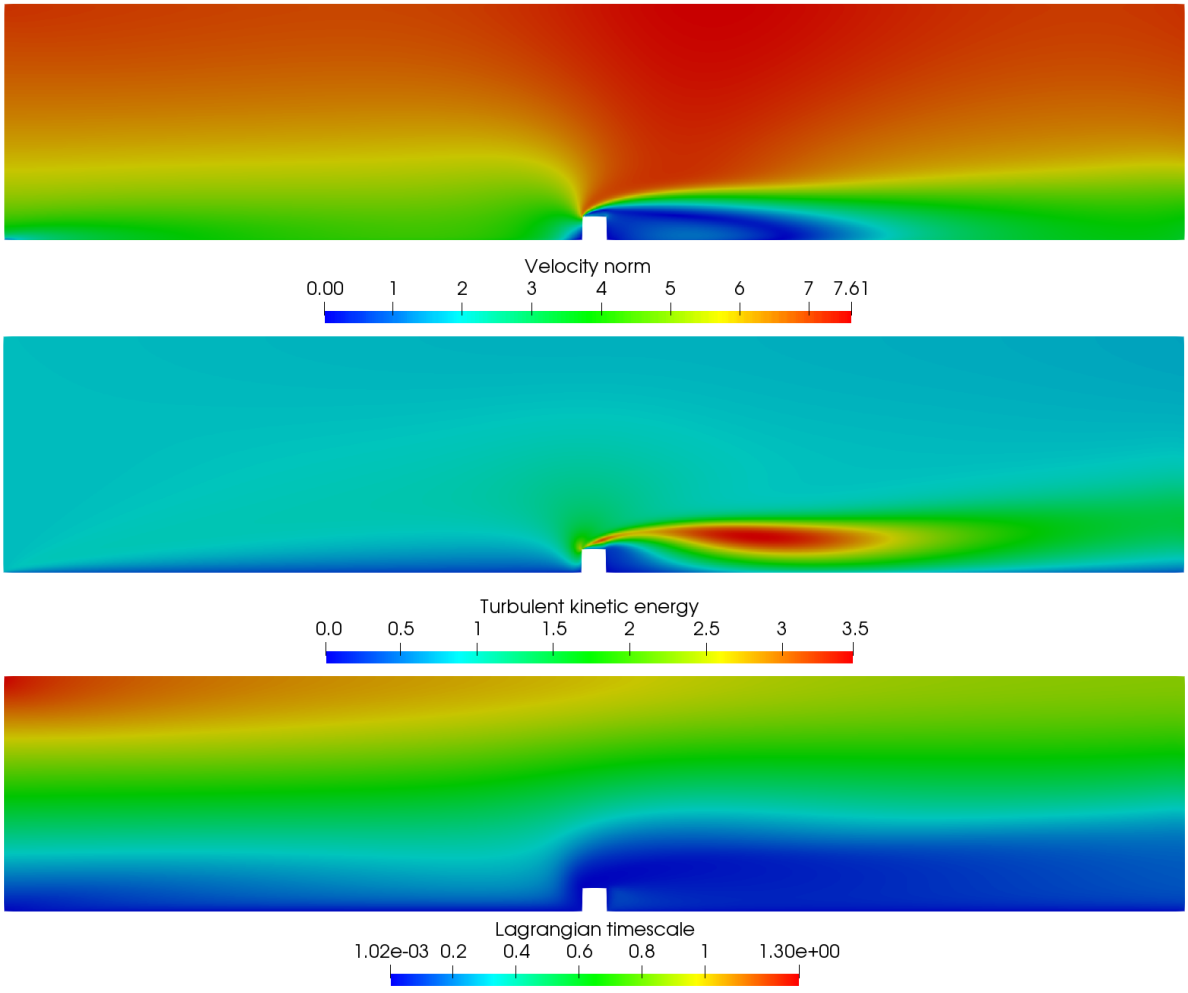

Figure 12: Isovalues of mean fluid fields for the case of the obstacle within a boundary layer. From top to bottom: velocity norm ($m.s^{-1}$), turbulent kinetic energy ($m^2.s^{-2}$), Lagrangian timescale (s).

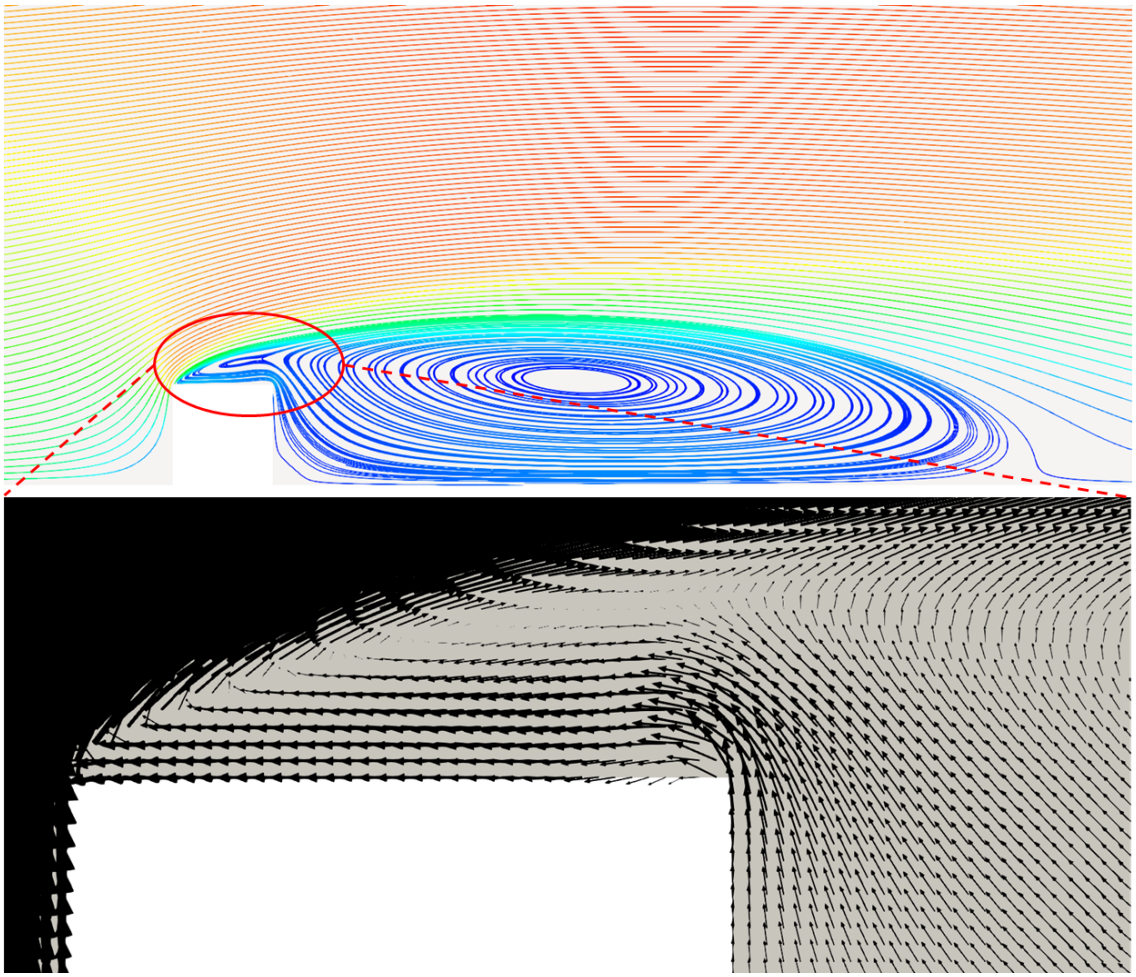

Figure 13: Mean fluid velocity field for the case of the flow around an obstacle within a boundary layer. Figure at the top shows the velocity streamlines. The close view around the obstacle displayed in the bottom figure reveals the complexity of the flow patterns, with a double recirculation on top and downstream of the obstacle.

izing a large number of particles ($N_{ini} = 2\,928\,000$) in the domain with a uniform position distribution to respect incompressibility. In each cell, particle velocities were initialized by sampling in a Gaussian distribution determined by the local value of the mean fluid velocity and second-order moments (the local value of the Reynolds-stress tensor). Unlike the infinite channel flow situation, this is a case with exit and inlet sections but with no periodic conditions. Therefore, during each time step, a number of fluid particles ($N_{inlet} = 352$) are injected through the inlet section, according to the profile of the inlet mass flow rate. This number corresponds to the following ratio: $\langle c \rangle \, Q \, \Delta t / m_p$, where Q is the global fluid flow rate at the inlet, $\langle c \rangle$ the expected mean concentration given the particle initialization, m_p the (fictitious) mass of each particle and Δt the time step used for the calculation. Simulations were run for a long-enough time for particles to cross the domain and mix while ensuring that the memory of these initial conditions is lost and do not influence final numerical outcomes. Nevertheless, this initialization is useful to avoid the time-consuming explicit simulation of the transient period where particles have to fill the whole domain and acts as an accelerator of convergence. When a steady-state is reached, a typical number of particles present in the domain is in the order of $N = 3\,000\,000$, *i.e.*, about 4 particles per cell. Therefore, to extract reliable statistics, a time-averaging procedure was applied as in the mixing layer case. In order to ensure that results are independent of the number of samples, time averaging was used for a large number of time steps, even up to 200 000 time steps (which means that, on average, statistics are, in that case, estimated with around 800 000 particles in each cell).

Note that for this case, no typical scales can be used in the whole domain, as u_* is not a constant and there is no self-similarity. Therefore, apart from the mean concentrations, plots are displayed in terms of dimensional variables.

3.3.3. Results for particle concentration

As for the mixing layer and infinite channel cases, the mean particle concentration follows from the choice of numerical parameters but the relevant variable is the normalized particle concentration. Resulting particle concentration fields are shown in Fig. 14. From the upper part of this figure, it is seen that a uniform particle concentration is obtained throughout the whole domain when the pressure-gradient term is correctly accounted for in the SLM. For a more precise and quantitative analysis, it is best to extract profiles of the normalized particle concentration at various longitudinal positions. To that effect, five profiles are taken along the vertical direction at various downstream distances from the inlet section, as shown in Fig. 15. Given the complex flow pattern over the obstacle, three profiles are chosen in this area, while the first profile is taken upstream of the obstacle (but sufficiently far from the inlet for fully-developed channel flow conditions to exist) and the last one is at the end of the domain downstream of the obstacle.

For the complete form of the SLM, the five selected profiles of the normalized concentration are shown in Fig. 16a, which confirms that a truly well-mixed condition is obtained since all the different profiles remain fairly constant, apart from some fluctuations inherent to particle stochastic simulations. Given the challenging flow structure on the top of

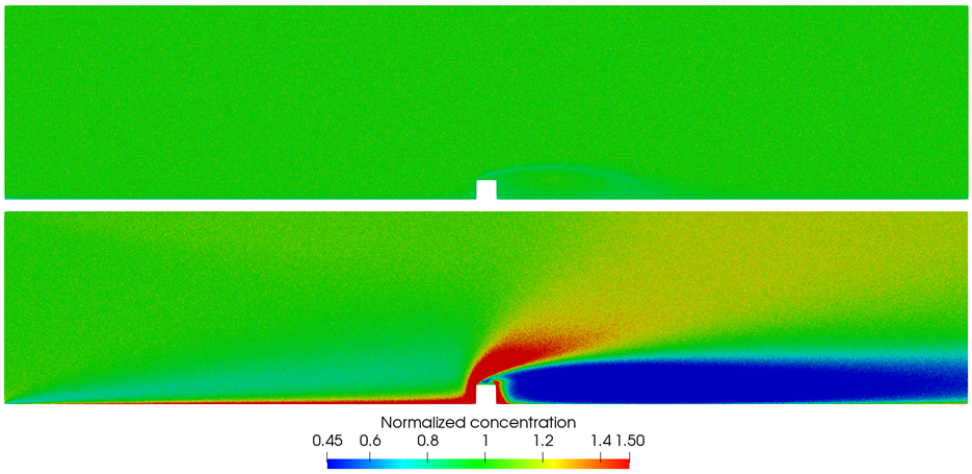

Figure 14: Particle normalized concentration field $c/\langle c \rangle$ for the case of flow around an obstacle within a boundary layer. From top to bottom: with and without the mean pressure-gradient term, respectively.

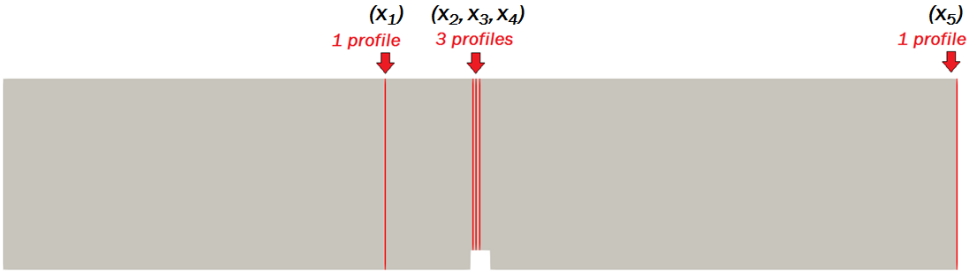

Figure 15: Position of the profiles for the case of the obstacle within a boundary layer. Five profiles are extracted: one upstream the obstacle (x_1), three in the critical region of the top of the obstacle (x_2, x_3 and x_4) and one near the outlet of the domain (x_5). Exact x coordinates of the profiles are: $x_1 = 2.00\ m$, $x_2 = 2.46\ m$, $x_3 = 2.48\ m$, $x_4 = 2.50\ m$, $x_5 = 5.00\ m$.

the obstacle, the fact that the normalized particle concentration remains equal to 1 is a noteworthy result. The global spatial error, defined as in Eq. (19), is 5.06% at the end of the calculation and is therefore satisfactorily low.

However, when the mean pressure-gradient term is not taken into account in the SLM, a completely different picture emerges with marked deviations of particle concentration from uniformity. This is already revealed by the color isovalues shown in the lower part of Fig. 14, with strong accumulation upstream of the obstacle (where fluid streamline curvatures are important) and zones of depletion downstream of the obstacle (in the recirculation zone). When profiles of the normalized concentration are extracted at the same five locations, it appears from the plots in Fig. 16b that severe errors are present, with some values reaching as high as four times the correct one. In that case, the global error is measured as high as 52.8%. This is clearly an unacceptable level of error which invalidates such formulations of dispersion models.

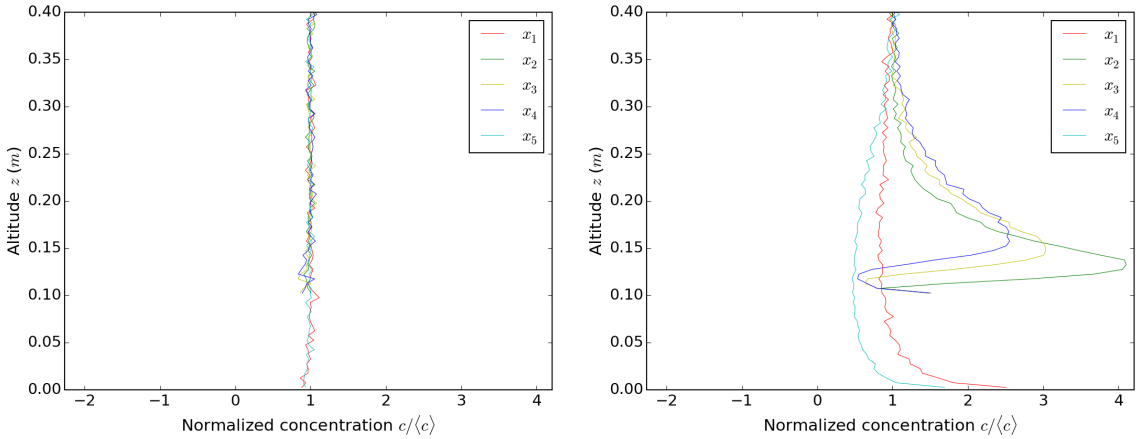

(a) With the mean pressure-gradient term (b) Without the mean pressure-gradient term

Figure 16: Vertical profiles of the particle normalized concentration at the five sections indicated in Fig. 15 for the case of the flow around an obstacle within a boundary layer. Comparison between the formulations with and without the mean pressure gradient in the SLM.

4. On the numerical implementation of incompressibility in particle models

The results of section 3 demonstrate that accounting for the mean pressure gradient in Langevin models ensures that no spurious drifts are present. As first put forward in Pope (1987), this is related to the respect of the mean continuity equation since, for incompressible flows, the mean pressure-gradient term acts as the mechanical force to guarantee that the mean velocity field is divergence free. Yet, in practical numerical implementations, its evaluation requires further consideration and two issues related to particle velocity and position corrections are now developed.

Correction of particle velocities. In stand-alone approaches, the mean pressure is calculated as the constraint needed to have $\mathrm{div}(\langle \mathbf{U}_p \rangle) = 0$ (cf. Minier and Pozorski (1999)). In hybrid Eulerian/Lagrangian formulations, it is easier to use directly the mean pressure gradient calculated by the Eulerian solver, say P^E, in the Langevin equations, so that Eq. (3b) can be expressed as

$$d\widetilde{U}_{p,i} = -\frac{1}{\rho_f}\frac{\partial P^E}{\partial x_i}\,dt + dM_i \ , \ \text{where } \langle dM_i \rangle = 0 \ , \tag{22}$$

where the notation $\widetilde{U}_{p,i}$ is used to indicate that this is a first estimation of particle velocities and where dM_i stands for the fluctuating part of the Langevin models which is not relevant for the present discussion. There are, however, always small differences between the numerical predictions of $\langle \mathbf{U}_f \rangle(t, \mathbf{x})$ and $\langle \widetilde{\mathbf{U}}_p \rangle(t, \mathbf{x})$. Consequently, Eq. (22) means that the resulting mean velocity field obtained from the Lagrangian solver $\langle \widetilde{\mathbf{U}}_p \rangle(t, \mathbf{x})$ is only approximately a divergence-free field. A more precise implementation consists in writing

$$dU_{p,i} = -\frac{1}{\rho_f}\frac{\partial P^E}{\partial x_i}\,dt - \frac{1}{\rho_f}\frac{\partial \delta P}{\partial x_i}\,dt + dM_i \ , \tag{23}$$

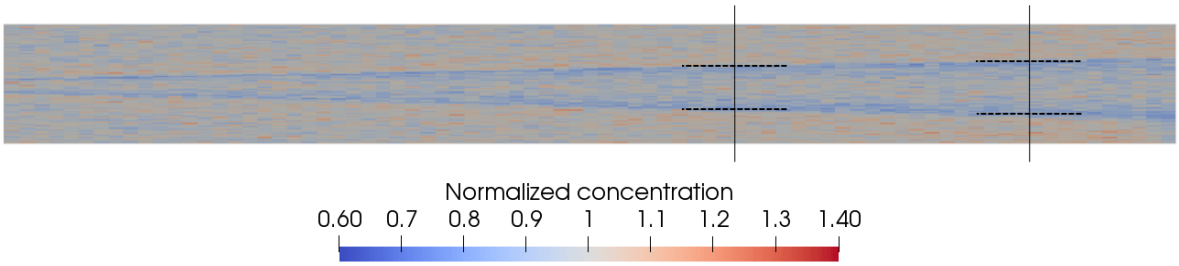

Figure 17: Concentration field in the mixing layer case without particle velocity correction (cf. Eq. (25)). A small depletion region develops downstream and is apparent at the edges of the mixing layer. The vertical lines which are indicated are used to extract and plot data at 7 m and 9 m, while the dashed lines locate the laminar-turbulent transitions at these downstream distances, cf. also Fig. 18.

where the pressure increments δP are computed to impose that $\mathrm{div}(\langle \mathbf{U}_p \rangle) = 0$. A classical numerical derivation based on the fractional time-step approach yields that δP is the solution of the Poisson equation

$$\frac{\Delta t}{\rho_f} \Delta(\delta P) = \mathrm{div}(\langle \widetilde{\mathbf{U}}_p \rangle) \ . \tag{24}$$

In order to test the importance of this correction, a short-cut method was used where particle velocities in a each cell are shifted so that the mean velocity field from the Lagrangian solver is equal to the one computed by the Eulerian solver. This is translated by the following correction: for each particle labeled $[k]$, with $k = 1, \ldots, N_{\mathbf{x}_m}$ where $N_{\mathbf{x}_m}$ is the number of particles located in the cell whose center is noted $\mathbf{x}_m$ (here m refers to the number of mesh cells), its instantaneous velocity is modified as

$$U_{p,i}^{[k]}(t) = \widetilde{U}_{p,i}^{[k]}(t) - \Big(\langle \widetilde{U}_{p,i} \rangle (t, \mathbf{x}_m) - \langle U_{f,i} \rangle (t, \mathbf{x}_m) \Big) \tag{25}$$

to enforce that $\langle U_{p,i} \rangle (t, \mathbf{x}) = \langle U_{f,i} \rangle (t, \mathbf{x})$ and retrieve a divergence-free mean velocity field.

The influence of this particle velocity correction can be estimated by considering the mixing layer case. When calculations are run without this velocity correction, it is seen from Fig. 17 that the normalized-concentration field is only approximately uniform with deviations from unity apparent at the edges of the mixing layer corresponding to the turbulent/laminar transition. This is confirmed by plotting concentration profiles along the lateral direction, as shown in Fig. 18a. However, when this velocity correction is applied, a better (and more stable) result is obtained, as revealed by the profiles in Fig. 18b.

Consequently, the particle velocity correction scheme was applied as the 'standard version' for the three examples studied in section 3. Note, therefore, that the profiles in Fig. 18b are the same of those in Fig. 6b, though a smaller scale for concentration values is used in Fig. 18b to bring out more clearly the respect of a uniform concentration.

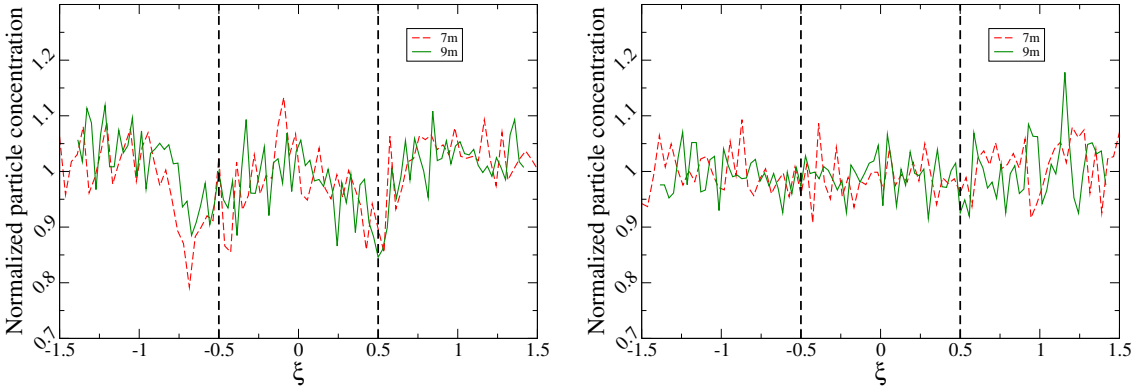

(a) Without particle velocity correction (b) With particle velocity correction

Figure 18: Profiles of the particle normalized concentration in the mixing layer at various distances from the inlet: comparison between the formulations without and with particle velocity correction (cf. Eq. (25)). The dashed lines correspond to the laminar-turbulent transitions indicated in Fig. 17.

Correction of particle positions. While it helps to improve mean velocity statistics, the above correction introduces a somewhat asymmetric treatment of particle positions and velocities, since the evolution equations for $(\mathbf{X}_p, \mathbf{U}_p)$ can be written as:

$$d\widetilde{X}_{p,i} = \widetilde{U}_{p,i}\, dt \ , \tag{26a}$$

$$dU_{p,i} = d\widetilde{U}_{p,i} - \frac{1}{\rho_f}\frac{\partial \delta P}{\partial x_i}\, dt \tag{26b}$$

where the same notation $\widetilde{\mathbf{X}}_p$ for particle positions is used to indicate that this is a first estimation. Eq. (26a) shows that particle positions are influenced by the velocity correction but only in a sequential manner: once particle velocities are corrected, particle positions are modified at the following time step. This loose coupling can be sufficient in some cases, such as the mixing layer and infinite channel flow cases, but can be limited for more complex flow patterns with flow reversals and recirculation. This is the situation met with the flow around the obstacle in the neutral boundary layer. For this reason, tighter coupling is needed between particle positions and velocities.

In stand-alone PDF approaches (see Minier and Pozorski (1999); Bernardin et al. (2009); Chauvin et al. (2010)), as well as in Smoothed Particle Hydrodynamics (SPH) simulations of incompressible flows (Szewc et al., 2012), this is done by introducing a specific correction on particle positions, so that the complete system can be represented by

$$dX_{p,i} = \widetilde{U}_{p,i}\, dt + \delta X_{p,i} \ , \tag{27a}$$

$$dU_{p,i} = d\widetilde{U}_{p,i} - \frac{1}{\rho_f}\frac{\partial \delta P}{\partial x_i}\, dt \ , \tag{27b}$$

where in Eq. (27a) the correction term $\delta X_{p,i}$, accounts for the integrated effect (within each time step) of the one acting on particle velocities in Eq. (27b). This particle correction

term is derived by stating that a uniform particle concentration field should be obtained. Expressing $\delta X_{p,i}$ as the integrated effect of a potential correcting field $\delta\phi$, *i.e.*, with $\delta X_{p,i} = \partial(\delta\phi)/\partial x_i \, \Delta t$, leads to the formulation of a second Poisson equation whose solution is this correcting potential $\delta\phi$. Further details on this numerical implementation with corrections on particle velocities and positions can be found in Minier and Pozorski (1999).

As for particle velocities, a short-cut method was used to assess whether such a complete treatment is needed. To that effect, particle positions are simply modified by adding a Brownian-like term to the particle position equation, so that we have now

$$dX_{p,i} = \widetilde{U}_{p,i}\, dt + \alpha\, dW_i' \ , \tag{28a}$$

$$dU_{p,i} = d\widetilde{U}_{p,i} - \frac{1}{\rho_f}\frac{\partial \delta P}{\partial x_i}\, dt \ , \tag{28b}$$

where α is a small parameter and $\mathbf{W}'$ a set of Wiener processes independent from the ones used in the Langevin model for particle velocities. This corresponds to applying a simple shifting term to particle positions, or a Laplacian term in the (Fokker-Planck type of) PDE governing the evolution of the particle concentration field.

In the case of the flow around the obstacle, this version was used to obtain the numerical results presented in section 3.3. In the simulations, the value of α had the same magnitude as the diffusion coefficient used to represent viscous effects (*i.e.*, $\alpha \approx$ 1-2 $\times \sqrt{2\nu}$ where ν is the fluid kinematic viscosity) but α remains nevertheless a numerical parameter in the present context. The effects of this particle correction scheme can be seen by comparing results on the particle concentration field with and without that term (cf. Figs. 19 and 20). Clearly, improved predictions are obtained when the correction term is applied. Given the simplified version used in Eq. (28a), this indicates that the complete formulation in terms of $\delta\phi$ as the solution of the corresponding Poisson equation needs to be introduced.

To sum up, two short-cut methods were used to reveal that the numerical implementation of the mean pressure-gradient term (coming from the Eulerian solver in hybrid formulations) should be supplemented with corrections both for particle velocities and positions. These correction terms have been proved necessary in stand-alone algorithms but should also be used in hybrid Eulerian/Lagrangian calculations.

5. Numerical assessment of the consistency between fluid and particle phases

In section 2.3, the consistency issue between turbulence models used in hybrid Eulerian/Lagrangian formulations was brought out. The relevance of this issue is now addressed from a numerical point of view by analyzing results obtained with the cases studied in section 3. Given that the flow around the obstacle is similar to the one in a channel flow in the region upstream of the obstacle, it was chosen to concentrate on the two more complex flow situations. This corresponds to the cases of the mixing layer (cf. section 3.1) and of the flow around the obstacle in a neutral boundary layer (cf. section 3.3), for results pertaining to the bulk of the flow while the issue of wall-conditions consistency is assessed by considering the infinite channel flow case (cf. section 3.2) later on.

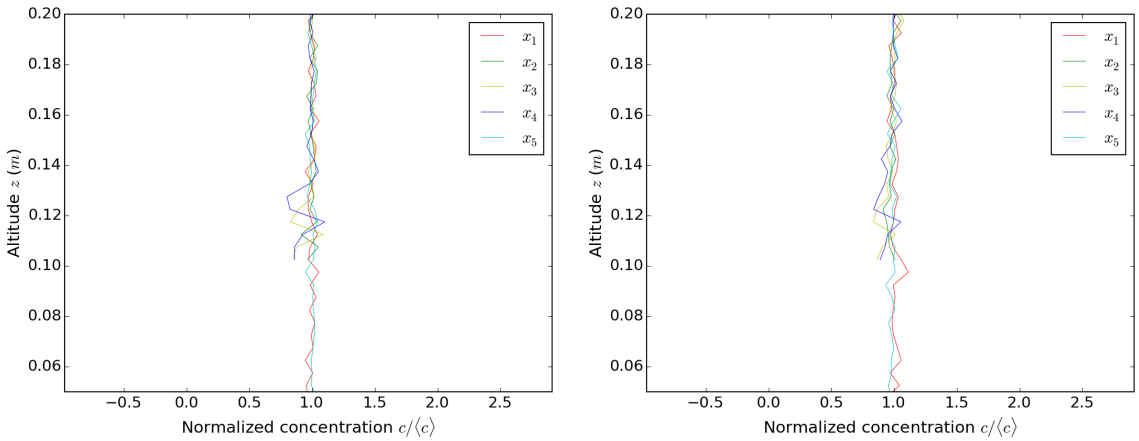

(a) Without particle position correction (b) With particle position correction

Figure 19: Vertical profiles of the particle normalized concentration at the five sections shown in Fig. 15 for the case of the flow around the obstacle within a boundary layer: comparison between the formulations with and without particle position correction, Eq. (28a). The particle velocity correction, Eq. (25), is applied in both formulations.

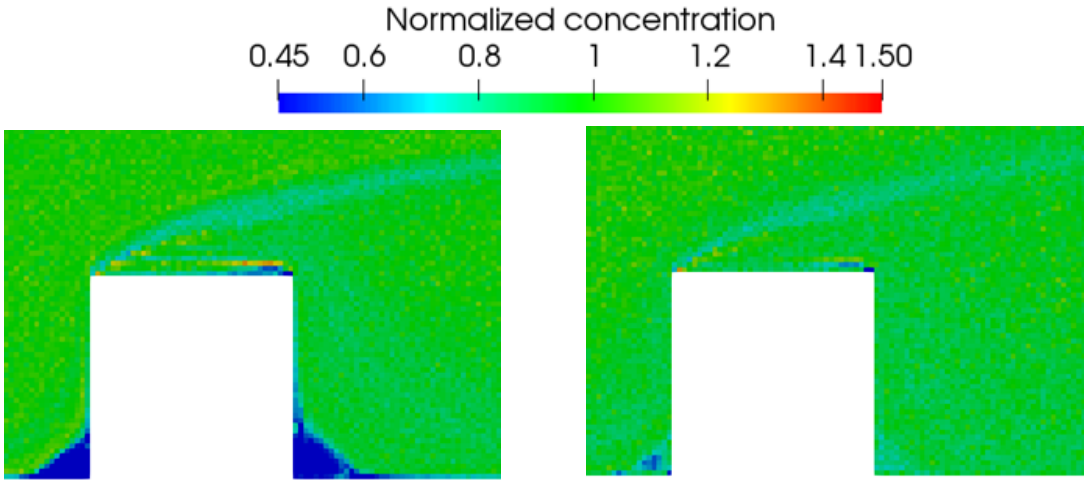

(a) Without particle position correction (b) With particle position correction

Figure 20: Zoom near the obstacle of the particle normalized concentration field for the case of the flow around obstacle within a boundary layer: comparison between the formulations without and with particle position correction, Eq. (28a). The particle velocity correction, Eq. (25), is applied in both formulations.

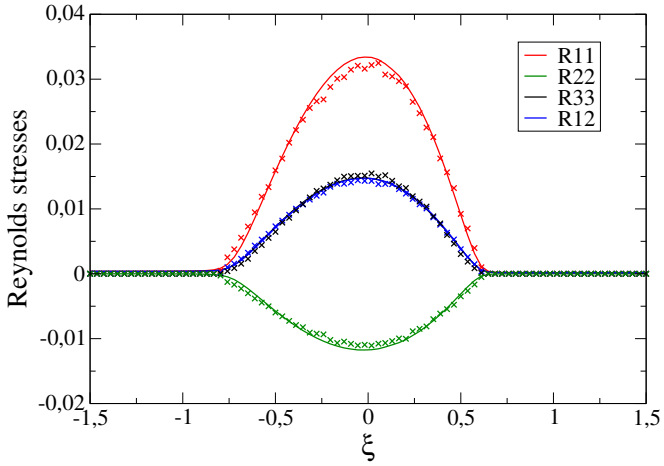

Figure 21: Profiles of the scaled Reynolds stresses in the self-similar regime (obtained here at 7 m) for the mixing layer case provided by the Eulerian solver (continuous lines) and the Lagrangian one (crosses) with the consistent hybrid Rotta model/SLM formulation. Both approaches yield nearly-identical predictions for the same second-order velocity moments.

It is important to remember that the aim is not to compare an 'Eulerian model' to a 'Lagrangian one' but to assess whether, in hybrid Eulerian/Lagrangian formulations, duplicate fields are indeed simulated as such, that is whether both predictions are identical. In that sense, inconsistency is revealed by discrepancies between numerical outcomes for mean fluid moments. Furthermore, since mean fluid velocity calculated by a CFD code are directly used in the return-to-equilibrium term of Langevin models (see the structure of the GLM, cf. Eq. (3b)) and given the numerical corrections detailed in section 4, consistency for the mean fluid velocity field is automatically ensured. Potential differences appear only at the level of second-order moments which are thus studied specifically here.

5.1. On the turbulence model consistency

We start with results obtained with the theoretically consistent hybrid formulation in which a second-order Rotta model is used in the Eulerian approach with the SLM for the Lagrangian one. Then, the effect of using a eddy-viscosity model, such as the $k-\epsilon$, for the Eulerian calculation is investigated.

In the mixing layer case, once the self-similar regime is reached, scaled Reynolds stresses are extracted from the Lagrangian calculation and compared to the ones from the Rotta model used in the CFD code (note that these results were already given in Fig. 5). Both predictions of the scaled non-zero second-order fluid velocity moments are shown in Fig. 21. It can be seen that the Reynolds stresses decrease as expected at the edges of the turbulent region where a turbulent/laminar transition is observed. More importantly for our present concern, it is clear that numerical results for the particle phase are in very good agreement with those for the fluid phase, indicating that consistency is achieved.

We now consider the case of the flow around an obstacle in a neutral boundary layer, which is more complex since it involves wall effects and flow recirculation. Following the

analysis in section 3.3, three zones (upstream, over, and downstream of the obstacle) are selected where vertical profiles are extracted. This is shown in Fig. 22 for the consistent hybrid Rotta-SLM formulation. It can be seen that the profiles computed through the Eulerian and Lagrangian approaches are quite similar, especially R_{33} where the identity is almost perfect. There are, however, small differences for R_{11} values, which is the longitudinal fluid kinetic energy. At that stage, it must recalled that, from a numerical point of view, consistency between Eulerian and Lagrangian approaches can not be perfectly enforced since the triple moment has to be modeled in the Eulerian formulation (usually through a Daly-Harlow closure) while it is treated without approximation by particle-based approaches. Over the obstacle, second-order moments are in a very good agreement, which is a noteworthy result given the possible difficulties caused by the strong recirculating flow patterns present in the region. In spite of small differences that still require further analysis, it can nevertheless be concluded that a quite satisfactory agreement between both Eulerian and Lagrangian results are obtained for these duplicate fields, which brings support for the overall hybrid formulation.

In order to illustrate the importance of consistent formulations, another simulation was performed using the first-order $k-\epsilon$ turbulence model for the Eulerian calculation. Results are shown in Fig. 23, which displays the turbulent kinetic energy vertical profiles at the same locations as the ones shown in Fig. 22. It is obvious that significant discrepancies are observed between predictions of the same physical quantity, proving that this hybrid formulation is inconsistent and, therefore, invalid for reliable predictions. Moreover, the resulting particle concentration field is also affected with non-negligible zones of depletion over the obstacle (see Fig. 24).

5.2. On the wall-boundary condition consistency

In this paragraph, we illustrate the effect of the wall-boundary conditions discussed in section 2.4 on fluid second-order velocity moments and, for that purpose, we consider the case of the infinite plane channel. Two calculations are performed: one with a wall-boundary condition corresponding to specular rebound ($U_{p,x}^{in} = U_{p,x}^{out}$ and $U_{p,y}^{in} = U_{p,y}^{out}$), and another one where the wall-boundary treatment consistent with the classical wall-function formulation is used (see Eqs. (11) in section 2.4).

The profiles of the non-zero Reynolds stresses are displayed in Fig. 25. The effect of using consistent wall-boundary conditions can clearly be observed: the agreement between the Reynolds-stress values extracted from the Eulerian and Lagrangian solvers is much better than when specular rebound is used. In particular, the improvement is notable for R_{11} and R_{13} with the difference between Eulerian and Lagrangian values being reduced by half. It can be seen that R_{33} is not affected, which makes sense since the normal velocity remains unchanged, see Eqs. (11). The difference between the resulting profiles of the shear stress R_{13} is noteworthy since this is the key element of near-wall turbulent boundary layers (also called constant-stress layers) when the viscous sublayer is bridged: applying a specular rebound yields a zero-flux condition for the mean longitudinal velocity component and a zero shear stress completely at variance with classical laws of wall-boundary layers

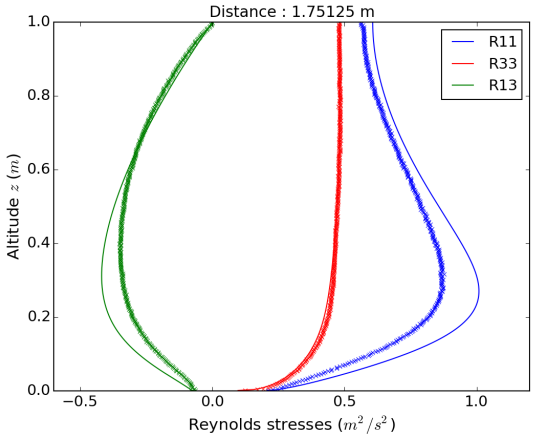

(a) Upstream of the obstacle

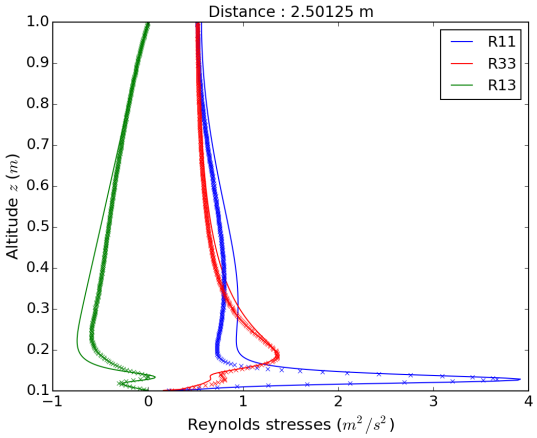

(b) Over the obstacle

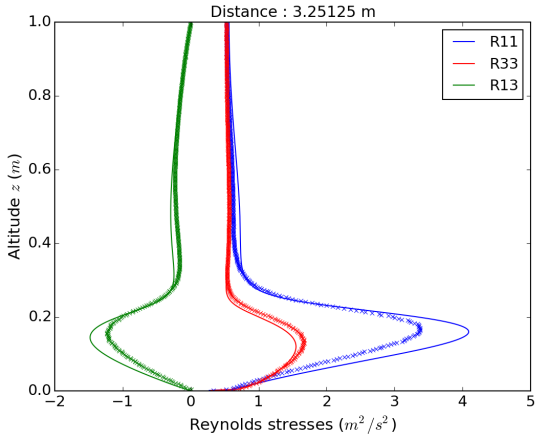

(c) Downstream of the obstacle

Figure 22: Reynolds stresses vertical profiles at various distances from the inlet obtained with the hybrid formulation Rotta model/SLM for the case of the flow around an obstacle within a boundary layer. The duplicate predictions correspond to the result of the Eulerian solver (continuous lines) and the Lagrangian one (crosses).

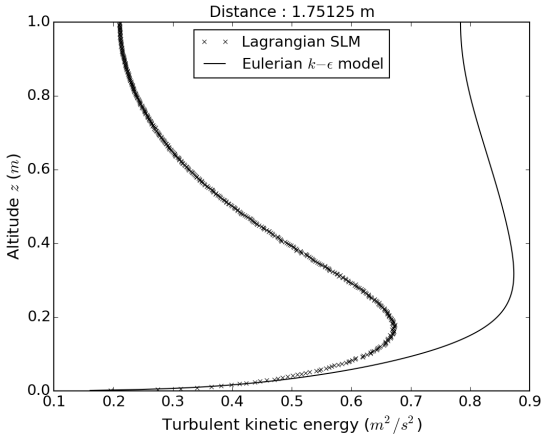

(a) Upstream of the obstacle

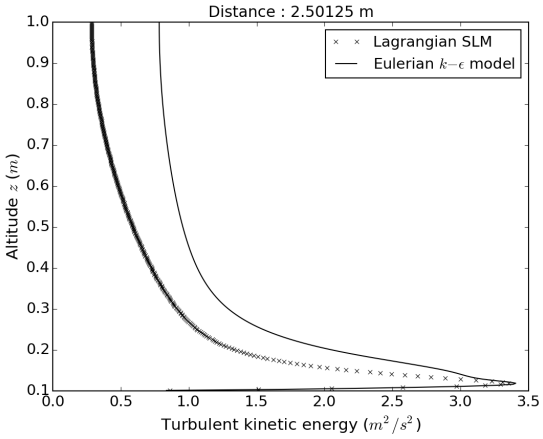

(b) Over the obstacle

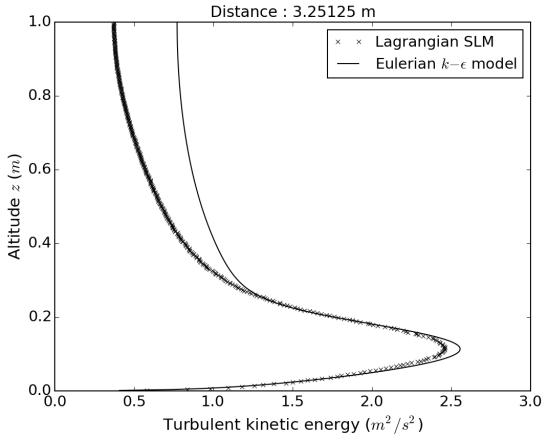

(c) Downstream of the obstacle

Figure 23: Turbulent kinetic energy vertical profiles at various distances from the inlet for the case of the flow around an obstacle within a boundary layer. A different hybrid formulation is used, with the $k-\epsilon$ model applied in the Eulerian solver while the SLM is retained in the Lagrangian one. This results in inconsistent predictions for the fluid kinetic energy by this hybrid method.

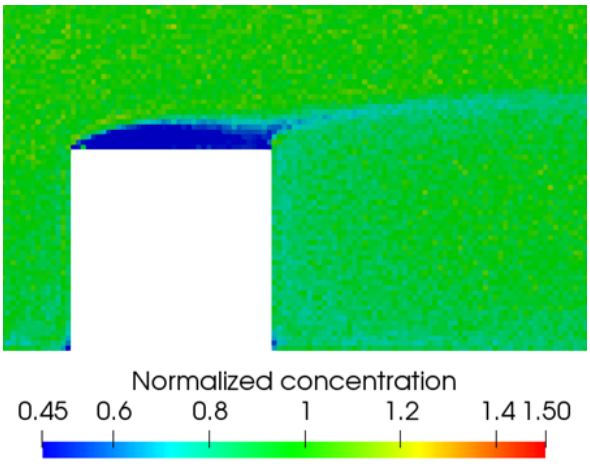

Figure 24: Zoom near the obstacle of the particle normalized concentration field for the case of the flow around obstacle within a boundary layer obtained with the inconsistent hybrid $k-\epsilon$ model/SLM formulation. Even with the particle correction schemes described in section 4, a depletion region appears on the top of the obstacle.

at high Reynolds-number turbulent flows, while a satisfactory behavior of the shear stress is retrieved with the complete boundary conditions in Eqs. (11).

In practical numerical formulations of wall-boundary conditions, specific discretizations are sometimes used. This is the case for the present implementation of wall-conditions in the CFD code *Code_Saturne* (where so-called two-velocity scale numerical implementations are used), which can explain remaining differences in the numerical outcomes. Further work needs to be done to ensure a full correspondence down to the actual numerical formulations. Nevertheless, it can be concluded that wall-boundary conditions are necessary in Lagrangian stochastic formulations and must be implemented consistently with the ones applied in the Eulerian solver when a hybrid formulation is used.

6. Conclusions and perspectives

The purpose of the present paper was to help the development and use of Lagrangian stochastic models for atmospheric dispersion applications by clarifying, through theoretical considerations and a range of numerical situations, the issues of the well-mixed condition and consistencies between duplicate fields in hybrid Eulerian/Lagrangian simulations.

First of all, it has been recalled that the respect of the well-mixed condition is ensured when the mean pressure-gradient term is correctly introduced as the mean drift term of Langevin models for the evolution of instantaneous fluid particle velocities, regardless of the details of the fluctuating part of these models. It is believed that this result is helpful for the development of physics-based stochastic models, since it allows to concentrate on the specific details of Langevin models (*i.e.*, the fluctuating part which governs the ability of a model to capture relevant timescales, etc.). This framework also simplifies the

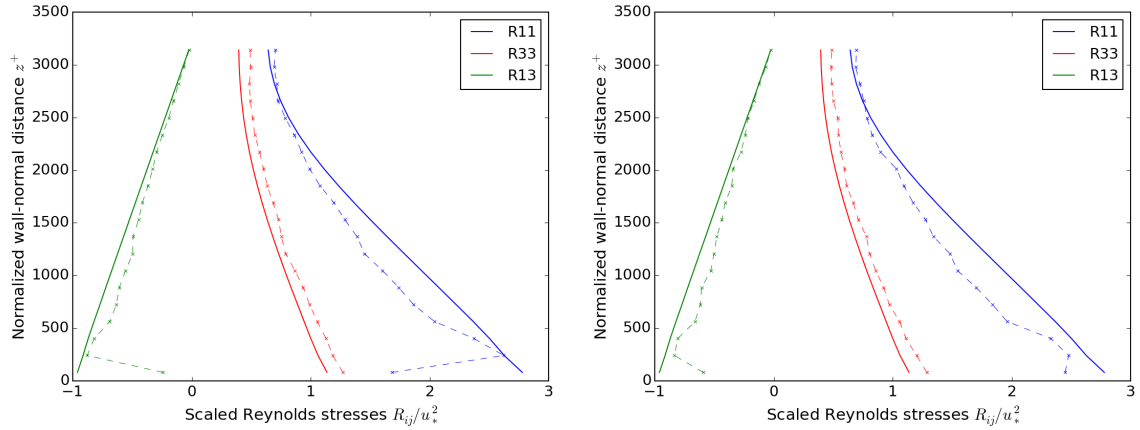

(a) Specular rebound (b) Wall-boundary condition Eq. (11)

Figure 25: Reynolds stresses vertical profiles for the case of the infinite plane channel: comparison between two versions of wall-boundary conditions with the consistent hybrid Rotta/SLM formulation. In both versions, consistency is assessed by checking the similarity of the predictions from the Eulerian solver (continuous lines) and the Lagrangian one (dashed crosses).

analysis of Langevin models by providing a one-way approach in which Eulerian PDFs are derived from Lagrangian ones (and not the other way around) while safeguarding that the resulting formulation is always consistent with the mean Navier-Stokes equation and the incompressibility condition.

With respect to the well-mixed criterion, the importance of including the mean pressure-gradient term has been demonstrated by the new results presented in this work which cover a range of challenging situations involving non-homogeneous, recirculating and wall-bounded turbulent flows. These examples confirm that the well-mixed condition is satisfied when the mean pressure gradient is correctly accounted for, while serious discrepancies, with zones of particle depletion and/or accumulation, result when this term is absent.

In particle-based models, the incompressibility constraint is translated into a double one: that the mean velocity derived from particle velocities be of zero divergence, and that the mean concentration derived from particle positions remain constant. In practical numerical implementations, this is reflected by a double correction, first with the introduction of the mean pressure-gradient term calculated from the zero-divergence condition of the mean flow and, second, by a correction step on particle positions. This formulation is valid for both stand-alone and hybrid Eulerian/Lagrangian numerical codes.

In practice, most applications for atmospheric dispersion studies are carried out with hybrid Eulerian/Lagrangian simulations, which are not mandatory but nevertheless helpful to provide free-of-statistical-noise mean fluid properties (such as the mean velocity field) from the Eulerian solver to the Lagrangian one. However, hybrid formulations raise consistency issues for mean fluid properties predicted both from the Eulerian and Lagrangian models. It is therefore of paramount importance to realize that the development of im-

proved Eulerian solvers, through advanced turbulence models, does not necessarily entail that Lagrangian predictions, based on a given Langevin model, will be improved. What is central is that both Eulerian and Lagrangian turbulence models be consistent. In that sense, a second interest of the present work is to bring out this issue for atmospheric studies and to reveal, through numerical simulations in a neutral boundary layer, the potentially-damaging errors induced when inconsistent turbulence models are used.

It is hoped that present results will be helpful to atmospheric models by allowing future theoretical and numerical efforts to be safely channeled towards improved predictions while ensuring that basic conditions and constraints are satisfied. Indeed, Lagrangian stochastic models have great interest for passive (as well as reactive) scalar modeling. For example, Bahlali et al. (2018) have considered point source dispersion and correctly captured the near- and far-field dispersive behaviors even when using a simple Langevin model. For future investigations, it will therefore be interesting to extend present consistent hybrid Eulerian/Lagrangian approaches to include scalar modeling based on more-advanced Generalized Langevin Model.

Appendix A. On the relation between instantaneous and fluctuating velocities for Langevin models

From the definition of the fluctuating velocity, we have:

$$dU'_{p,i} = dU_{p,i} - d\langle U_{f,i}\rangle \ . \tag{A.1}$$

Recalling that the fluid particle velocity is simply the value of the velocity field at the particle location, *i.e.*, $U_{p,i}(t) = U_{f,i}(t, \mathbf{X}_p(t))$, the differential of the mean velocity of the fluid along an instantaneous fluid particle trajectory is expressed by:

$$\frac{d\langle U_{f,i}\rangle}{dt} = \frac{\partial\langle U_{f,i}\rangle}{\partial t} + U_{p,j}\frac{\partial\langle U_{f,i}\rangle}{\partial x_j} \ , \tag{A.2}$$

from which it follows that

$$\frac{d\langle U_{f,i}\rangle}{dt} = \frac{\partial\langle U_{f,i}\rangle}{\partial t} + \langle U_{f,j}\rangle\frac{\partial\langle U_{f,i}\rangle}{\partial x_j} + U'_{p,j}\frac{\partial\langle U_{f,i}\rangle}{\partial x_j} \ . \tag{A.3}$$

On the other hand, the mean Navier-Stokes equations is (leaving out the mean viscosity term (at high Reynolds-number numbers):

$$\frac{\partial\langle U_{f,i}\rangle}{\partial t} + \langle U_{f,j}\rangle\frac{\partial\langle U_{f,i}\rangle}{\partial x_j} = -\frac{1}{\rho_f}\frac{\partial\langle P_f\rangle}{\partial x_i} - \frac{\partial\langle U'_{f,i}U'_{f,j}\rangle}{\partial x_j} \ . \tag{A.4}$$

Injecting this last equation into Eq. (A.3) gives:

$$\frac{d\langle U_{f,i}\rangle}{dt} = -\frac{1}{\rho_f}\frac{\partial\langle P_f\rangle}{\partial x_i} - \frac{\partial\langle U'_{f,i}U'_{f,j}\rangle}{\partial x_j} + U'_{p,j}\frac{\partial\langle U_{f,i}\rangle}{\partial x_j} \ , \tag{A.5}$$

which finally yields that:

$$dU'_{p,i} = dU_{p,i} + \left(\frac{1}{\rho_f}\frac{\partial\langle P_f\rangle}{\partial x_i} + \frac{\partial\langle U'_{f,i}U'_{f,j}\rangle}{\partial x_j} - U'_{p,j}\frac{\partial\langle U_{f,i}\rangle}{\partial x_j}\right)dt \ . \tag{A.6}$$

If we consider a Langevin model such as the GLM (cf. Eq. (3)), we obtain that:

$$\begin{aligned} dU'_{p,i} = -\frac{1}{\rho_f}\frac{\partial\langle P_f\rangle}{\partial x_i}dt - G_{ij}(U_{p,i} - \langle U_{f,i}\rangle)dt + \sqrt{C_0\epsilon_f}\,dW_i \\ + \left(\frac{1}{\rho_f}\frac{\partial\langle P_f\rangle}{\partial x_i} + \frac{\partial\langle U'_{f,i}U'_{f,j}\rangle}{\partial x_j} - U'_{p,j}\frac{\partial\langle U_{f,i}\rangle}{\partial x_j}\right)dt \end{aligned} \tag{A.7}$$

which, after simplification of the mean pressure-gradient term, gives:

$$dU'_{p,i} = \left(\frac{\partial\langle U'_{f,i}U'_{f,j}\rangle}{\partial x_j} - U'_{p,j}\frac{\partial\langle U_{f,i}\rangle}{\partial x_j}\right)dt - G_{ij}U'_{p,j}\,dt + \sqrt{C_0\epsilon_f}\,dW_i \ . \tag{A.8}$$

In the particular case of the SLM (cf. Eqs. (5)-(6)), we get therefore that:

$$dU'_{p,i} = \left(\frac{\partial\langle U'_{f,i}U'_{f,j}\rangle}{\partial x_j} - U'_{p,j}\frac{\partial\langle U_{f,i}\rangle}{\partial x_j}\right)dt - \frac{U'_{p,i}}{T_L}\,dt + \sqrt{C_0\epsilon_f}\,dW_i \ . \tag{A.9}$$

Appendix B. Demonstration of the $R_{ij} - \epsilon$ Rotta/SLM consistency

The PDF transport equation incorporating the GLM writes as follows:

$$\frac{\partial f}{\partial t} + V_i \frac{\partial f}{\partial x_i} - \frac{1}{\rho_f} \frac{\partial \langle P_f \rangle}{\partial x_i} \frac{\partial f}{\partial V_i} = -\frac{\partial}{\partial V_i} \left[f G_{ij} (V_j - \langle U_{f,j} \rangle) \right] + \frac{1}{2} C_0 \epsilon_f \frac{\partial^2 f}{\partial V_i V_j} \ . \tag{B.1}$$

Note that this equation is satisfied first by the Lagrangian PDF, $f_L(t; \mathbf{x}, \mathbf{V})$, from which the one satisfied by the Eulerian PDF, $f_E(t, \mathbf{x}; \mathbf{V})$, is derived (since the Eulerian PDF is defined as the Lagrangian conditioned on a given location). For incompressible flows, the PDF of particle location is a constant and f_E, which is then proportional to f_L, satisfies the same PDF equation as f_L. With these relations in mind, the index is dropped in the following derivations to keep simple notations. From Eq. (B.1), it is then straightforward to derive moments of the velocity field since, for any moment of order m, we have

$$\langle U_{f,i}^m(t, \mathbf{x}) \rangle = \int V_i^m \, f(t, \mathbf{x}; \mathbf{V}) \, d\mathbf{V} \ . \tag{B.2}$$

The equation for the first velocity moment is obtained by multiplying Eq. (B.1) by V_j and integrating over velocity space, from which we exactly retrieve the mean Navier-Stokes momentum equation. As for the second moment, multiplying Eq. (B.1) this time by $V_j V_k$ and integrating over $\mathbf{V}$ yields the following equation (after some manipulations to substract the one for $\langle U_{f,i} \rangle \langle U_{f,j} \rangle$):

$$\frac{D \langle U'_{f,i} U'_{f,j} \rangle}{Dt} + \frac{\partial \langle U'_{f,i} U'_{f,j} U'_{f,k} \rangle}{\partial x_k} = P_{ij} + G_{ik} \langle U'_{f,j} U'_{f,k} \rangle + G_{jk} \langle U'_{f,i} U'_{f,k} \rangle + C_0 \epsilon_f \delta_{ij} \tag{B.3}$$

where $D/Dt = \partial/\partial t + \langle U_{f,j} \rangle \partial/\partial x_j$ stands for transport by the mean velocity and where P_{ij} is the production tensor:

$$P_{ij} = -\langle U'_{f,i} U'_{f,k} \rangle \frac{\partial \langle U_{f,j} \rangle}{\partial x_k} - \langle U'_{f,j} U'_{f,k} \rangle \frac{\partial \langle U_{f,i} \rangle}{\partial x_k} \ . \tag{B.4}$$

As explained by Pope (2000), the first three terms of Eq. (B.3) are exact. It is interesting to compare this equation to the exact Reynolds-stress equations, which are:

$$\frac{D \langle U'_{f,i} U'_{f,j} \rangle}{Dt} + \frac{\partial T_{kij}}{\partial x_k} = P_{ij} + R_{ij} - \epsilon_{f,ij} \tag{B.5}$$

where:

$$T_{kij} = \langle U'_{f,i} U'_{f,j} U'_{f,k} \rangle - \nu \frac{\partial \langle U'_{f,i} U'_{f,j} \rangle}{\partial x_k} + \frac{1}{\rho_f} \langle U'_{f,i} P'_f \rangle \delta_{jk} + \frac{1}{\rho_f} \langle U'_{f,j} P'_f \rangle \delta_{ik} \tag{B.6}$$

and:

$$R_{ij} = \left\langle \frac{P'_f}{\rho_f} \left(\frac{\partial U'_{f,i}}{\partial x_j} + \frac{\partial U'_{f,j}}{\partial x_i} \right) \right\rangle \ . \tag{B.7}$$

By identifying Eq. (B.1) to (B.5) and if we neglect viscous and pressure transport (last three terms of Eq. (B.6)), we obtain:

$$R_{ij} - \epsilon_{f,ij} = G_{ik}\langle U'_{f,j}U'_{f,k}\rangle + G_{jk}\langle U'_{f,i}U'_{f,k}\rangle + C_0\epsilon_f\delta_{ij} \ . \tag{B.8}$$

Assuming dissipation to be isotropic (Pope, 2000) yields:

$$R_{ij} = G_{ik}\langle U'_{f,j}U'_{f,k}\rangle + G_{jk}\langle U'_{f,i}U'_{f,k}\rangle + (\frac{2}{3} + C_0)\epsilon_f\delta_{ij} \ . \tag{B.9}$$

Now, if we consider the SLM equation, *i.e.*, $G_{ij} = -(\frac{1}{2} + \frac{3}{4}C_0)\frac{\epsilon_f}{k}\delta_{ij}$, we obtain:

$$R_{ij} = -(1 + \frac{3}{2}C_0)\,\frac{\epsilon_f}{k_f}\left(\langle U'_{f,i}U'_{f,j}\rangle - \frac{2}{3}k_f\delta_{ij}\right) \ , \tag{B.10}$$

which shows that the SLM corresponds to the Rotta model, with $C_R = 1 + \frac{3}{2}C_0$ as the 'Rotta coefficient'.

Appendix C. Estimation of the Monte Carlo error

Let us assume first that we simulate only one particle. Let $c_{j,i}$ be the random variable associated with particle $j \in \mathbb{N}^*$ such that:

$$\begin{cases} c_{j,i} = 0 & \text{if particle } j \text{ is not in cell } i \\ c_{j,i} = \dfrac{v_p}{v_i} & \text{if particle } j \text{ is in cell } i \end{cases} \tag{C.1}$$

where v_p is the (fictious) volume of particle j and v_i the volume of cell i, $i \in \mathbb{N}^*$.

We can then deduce the spatial mean and variance values of $c_{j,i}$ as follows:

$$\langle c_{j,i} \rangle = \frac{1}{N_{cells}} \sum_{k=1}^{N_{cells}} c_{j,k} = \frac{c_{j,i}}{N_{cells}} \tag{C.2}$$

and (unbiased estimation of variance):

$$\begin{array}{ll} \sigma^2_{c_{j,i}} & = \frac{1}{N_{cells}} \sum_{k=1}^{N_{cells}} (c_{j,k} - \langle c_{j,k} \rangle)^2 \\ & = \frac{1}{N_{cells}-1} \left[\langle c_{j,i} \rangle^2 (N_{cells} - 1) + (c_{j,i} - \langle c_{j,i} \rangle)^2 \right] \\ & = \frac{1}{N_{cells}-1} \left[\langle c_{j,i} \rangle^2 (N_{cells} - 1) + (N_{cells} \langle c_{j,i} \rangle - \langle c_{j,i} \rangle)^2 \right] \\ & = \frac{\langle c_{j,i} \rangle^2}{N_{cells}-1} (N_{cells} - 1)(1 + N_{cells} - 1) \end{array} \tag{C.3}$$

which yields:

$$\sigma^2_{c_{j,i}} = \langle c_{j,i} \rangle^2 N_{cells} \ . \tag{C.4}$$

Now, let us assume we simulate N particles. Let $X_{N,i}$ be the random variable such that:

$$X_{N,i} = \sum_{j=1}^{N} c_{j,i} \ . \tag{C.5}$$

$X_{N,i}$ represents the concentration in cell i associated with the ensemble of the N particles. Since $\{c_{j,i}\}_{\{j=1..N\}}$ is a sequence of independent and identically distributed random variables, then the central limit theorem applies and the spatial mean and variance of $X_{N,i}$ write as follows:

$$\langle X_{N,i} \rangle = N \langle c_{j,i} \rangle \ , \tag{C.6}$$

and:

$$\sigma^2_{X_{N,i}} = N \sigma^2_{c_{j,i}} = N \langle c_{j,i} \rangle^2 N_{cells} \tag{C.7}$$

Normalizing the standard deviation of $X_{N,i}$ by its mean, we deduce the following formula:

$$\frac{\sigma_{X_{N,i}}}{\langle X_{N,i} \rangle} = \frac{\sqrt{N}\sqrt{N_{cells}}}{N} \tag{C.8}$$

hence:

$$\frac{\sigma_{X_{N,i}}}{\langle X_{N,i} \rangle} = \sqrt{\frac{N_{cells}}{N}} \ . \tag{C.9}$$

We deduce from this formula that the normalized standard deviation depends on the ratio between the number of particles simulated N and the number of cells N_{cells}. If $N \to \infty$, this standard deviation tends to 0. This result is coherent because if an infinity of particles were simulated, there would be no more variability of their number between the cells since there would also be an infinity in each.

It is worth noting that this error can also be seen as the deviation from a Poisson repartition. Indeed, as we consider an ensemble of discrete particles uniformly distributed in the domain, then the number of particles $N_{k,i}$ within a given cell i can be considered a Poisson random variable, whose average is $\lambda = N/N_{cells}$. The probability of observing $N_{k,i}$ particles in cell i is then given by the following equation:

$$P(N_{k,i}) = e^{-\lambda} \frac{\lambda^{N_{k,i}}}{N_{k,i}!} \ . \tag{C.10}$$

The expected value and variance of such a Poisson-distributed random variable are by definition both equal to λ, hence:

$$\frac{\sigma_{N_{k,i}}}{\langle N_{k,i} \rangle} = \frac{\sqrt{\lambda}}{\lambda} = \frac{1}{\sqrt{\lambda}} = \sqrt{\frac{N_{cells}}{N}} \ . \tag{C.11}$$

As the random variables $X_{N,i}$ and $N_{k,i}$ are proportional ($X_{N,i} = N_{k,i} v_p / v_i$), same conclusion as through Eq. (C.9) is retrieved.

References

Alessandrini, S., Ferrero, E., 2009. A hybrid Lagrangian–Eulerian particle model for reacting pollutant dispersion in non-homogeneous non-isotropic turbulence. Physica A: Statistical Mechanics and its Applications 388 (8), 1375–1387.

Archambeau, F., Méchitoua, N., Sakiz, M., 2004. Code Saturne: A Finite Volume Code for the computation of turbulent incompressible flows - Industrial applications. International Journal on Finite Volumes 1 (1), http://code–saturne.org.

Bahlali, M. L., Dupont, E., Carissimo, B., 2018. A hybrid CFD RANS/Lagrangian approach to model atmospheric dispersion of pollutants in complex urban geometries. Submitted to International Journal of Environment and Pollution.

Bernardin, F., Bossy, M., Chauvin, C., Drobinski, P., Rousseau, A., Salameh, T., 2009. Stochastic downscaling method: application to wind refinement. Stochastic Environmental Research and Risk Assessment 23 (6), 851–859.

Borgas, M. S., Flesch, T. K., Sawford, B. L., 1997. Turbulent dispersion with broken reflectional symmetry. Journal of Fluid Mechanics 332, 141–156.

Cassiani, M., Franzese, P., Giostra, U., 2005a. A PDF micromixing model of dispersion for atmospheric flow. Part I: development of the model, application to homogeneous turbulence and to neutral boundary layer. Atmospheric Environment 39 (8), 1457–1469.

Cassiani, M., Franzese, P., Giostra, U., 2005b. A PDF micromixing model of dispersion for atmospheric flow. Part II: application to convective boundary layer. Atmospheric Environment 39 (8), 1471–1479.

Cassiani, M., Radicchi, A., Albertson, J. D., 2007. Modelling of concentration fluctuations in canopy turbulence. Boundary-Layer Meteorology 122 (3), 655–681.

Champagne, F. H., Pao, Y. H., Wygnanski, I. J., 1976. On the two-dimensional mixing region. Journal of Fluid Mechanics 74 (2), 209–250.

Chauvin, C., Bernardin, F., Bossy, M., Rousseau, A., 2010. Wind simulation refinement: some new challenges for particle methods. In: Progress in Industrial Mathematics at ECMI 2008. Springer, pp. 765–770.

Chibbaro, S., Minier, J.-P., 2011. A note on the consistency of hybrid Eulerian/Lagrangian approach to multiphase flows. International Journal of Multiphase Flow 37 (3), 293–297.

De Baas, A. F., Van Dop, H., Nieuwstadt, F., 1986. An application of the Langevin equation for inhomogeneous conditions to dispersion in a convective boundary layer. Quarterly Journal of the Royal Meteorological Society 112 (471), 165–180.

Dreeben, T. D., Pope, S. B., 1997. Probability density function and Reynolds-stress modeling of near-wall turbulent flows. Physics of Fluids 9 (1), 154–163.

Franzese, P., 2003. Lagrangian stochastic modeling of a fluctuating plume in the convective boundary layer. Atmospheric Environment 37 (12), 1691–1701.

Gardiner, C. W., 1985. Handbook of stochastic methods for physics, chemistry and the natural sciences. Springer.

Lin, J. C., Gerbig, C., 2013. How can we satisfy the well-mixed criterion in highly inhomogeneous flows? a practical approach. Lagrangian Modeling of the Atmosphere, 59–70.

Minier, J.-P., 2015. On Lagrangian stochastic methods for turbulent polydisperse two-phase reactive flows. Progress in Energy and Combustion Science 50, 1–62.

Minier, J.-P., 2016. Statistical descriptions of polydisperse turbulent two-phase flows. Physics Reports 665, 1–122.

Minier, J.-P., Chibbaro, S., Pope, S. B., 2014. Guidelines for the formulation of Lagrangian stochastic models for particle simulations of single-phase and dispersed two-phase turbulent flows. Physics of Fluids 26 (11), 113303.

Minier, J.-P., Peirano, E., 2001. The PDF approach to turbulent polydispersed two-phase flows. Physics Reports 352 (1), 1–214.

Minier, J.-P., Pozorski, J., 1999. Wall-boundary conditions in probability density function methods and application to a turbulent channel flow. Physics of Fluids 11 (9), 2632–2644.

Monin, A. S., Yaglom, A. M., 1971. Statistical fluid dynamics. MIT Press, Cambridge.

Öttinger, H. C., 1996. Stochastic processes in polymeric fluids: tools and examples for developing simulation algorithms. Springer.

Peirano, E., Chibbaro, S., Pozorski, J., Minier, J.-P., 2006. Mean-field/PDF numerical approach for polydispersed turbulent two-phase flows. Progress in Energy and Combustion Science 32 (3), 315–371.

Pope, S. B., 1985. PDF methods for turbulent reactive flows. Progress in Energy and Combustion Science 11 (2), 119–192.

Pope, S. B., 1987. Consistency conditions for random-walk models of turbulent dispersion. Physics of Fluids 30 (8), 2374–2379.

Pope, S. B., 1991. Computations of turbulent combustion: progress and challenges. In: Symposium (International) on Combustion. Vol. 23. Elsevier, pp. 591–612.

Pope, S. B., 1994a. Lagrangian PDF methods for turbulent flows. Annual Review of Fluid Mechanics 26 (1), 23–63.

Pope, S. B., 1994b. On the relationship between stochastic Lagrangian models of turbulence and second-moment closures. Physics of Fluids 6 (2), 973–985.

Pope, S. B., 2000. Turbulent flows. Cambridge Univ. Press.

Sawford, B., 1986. Generalized random forcing in random-walk turbulent dispersion models. Physics of Fluids 29 (11), 3582–3585.

Sawford, B. L., 1985. Lagrangian statistical simulation of concentration mean and fluctuation fields. Journal of Climate and Applied Meteorology 24 (11), 1152–1166.

Sawford, B. L., Guest, F. M., 1988. Uniqueness and universality of Lagrangian stochastic models of turbulent dispersion. In: 8th Symposium on Turbulence and Diffusion. Vol. 1. pp. 96–99.

Stohl, A., Forster, C., Frank, A., Seibert, P., Wotawa, G., 2005. The Lagrangian particle dispersion model FLEXPART version 6.2. Atmospheric Chemistry and Physics 5 (9), 2461–2474.

Szewc, K., Pozorski, J., Minier, J.-P., 2012. Analysis of the incompressibility constraint in the smoothed particle hydrodynamics method. International Journal for Numerical Methods in Engineering 92 (4), 343–369.

Thomson, D. J., 1987. Criteria for the selection of stochastic models of particle trajectories in turbulent flows. Journal of Fluid Mechanics 180, 529–556.

Tinarelli, G., Mortarini, L., Castelli, S. T., Carlino, G., Moussafir, J., Olry, C., Armand, P., Anfossi, D., 2013. Review and validation of MicroSpray, a Lagrangian particle model of turbulent dispersion. Lagrangian Modeling of the Atmosphere, 311–328.

Van Dop, H., Nieuwstadt, F. T. M., Hunt, J. C. R., 1985. Random walk models for particle displacements in inhomogeneous unsteady turbulent flows. Physics of fluids 28 (6), 1639–1653.

Wilson, J. D., Sawford, B. L., 1996. Review of Lagrangian stochastic models for trajectories in the turbulent atmosphere. Springer.

Wilson, J. D., Thurtell, G. W., Kidd, G. E., 1981. Numerical simulation of particle trajectories in inhomogeneous turbulence, III: Comparison of predictions with experimental data for the atmospheric surface layer. Boundary-Layer Meteorology 21 (4), 443–463.

5.2 Complément

Suite à une demande spécifique d'EDF, une autre simulation relative au critère de mélange homogène a été réalisée, pour le cas de l'obstacle au sein d'une couche limite neutre. Pour cette nouvelle simulation, les paramètres suivants ont été modifiés :

— Les dimensions du domaine ont toutes été multipliées par 100 : le domaine est à présent de 500 m de longueur, de 100 m de hauteur, et l'obstacle est de taille 10 × 10 m.

— Au niveau du sol, une condition de paroi rugueuse a été imposée à la place de la paroi lisse, avec une valeur de rugosité de 10 cm.

— La condition limite au sommet du domaine, qui était une symétrie dans l'article Bahlali et al. (2018c), a été changée pour une entrée avec conditions de Dirichlet imposées pour la vitesse moyenne et le tenseur R_{ij}. Ceci afin d'imposer le flux correct de quantité de mouvement au sommet.

Le champ de concentration normalisé par la valeur moyenne attendue $c/\langle c \rangle$ obtenu est montré en Figure 5.1, avec une vue globale du domaine et un zoom autour de l'obstacle.

Nous observons une concentration uniforme dans tout le domaine, sauf au niveau de la zone située juste au-dessus de l'obstacle, où un puits de particules s'est formé. Pour une analyse plus précise, dans la Figure 5.2, nous présentons les profils verticaux de concentration normalisée extraits à cinq différentes distances dans la direction longitudinale. Les distances choisies pour les profils sont les mêmes (multipliées par 100) que pour le cas présenté dans l'article Bahlali et al. (2018c) reproduit en section 5.1 du présent chapitre, et le lecteur peut ainsi se référer à la Figure 15 de cet article pour retrouver la localisation des profils. Pour rappel, trois profils sont situés dans la zone critique au-dessus de l'obstacle, un profil est situé en amont de l'obstacle et le dernier se trouve en sortie de domaine.

Nous observons en Figure 5.2 que les cinq profils de concentration normalisée restent relativement constants, excepté à l'approche de l'obstacle où il existe une chute brutale des concentrations, correspondant au puits de particules précédemment mentionné. Plus d'investigations sont nécessaires sur ce sujet. Néanmoins, nous pouvons proposer une première analyse en Figure 5.3 en comparant les champs d'énergie cinétique turbulente autour de l'obstacle, par rapport au cas d'une paroi à très faible rugosité ($z_0 = 0.0025$ m) – cas dans lequel nous n'observons pas de puits de particules (non montré ici).

Sur la Figure 5.3, nous observons des niveaux d'énergie cinétique turbulente bien plus importants avec la configuration $z_0 = 0.1$ m, en particulier au niveau du coin

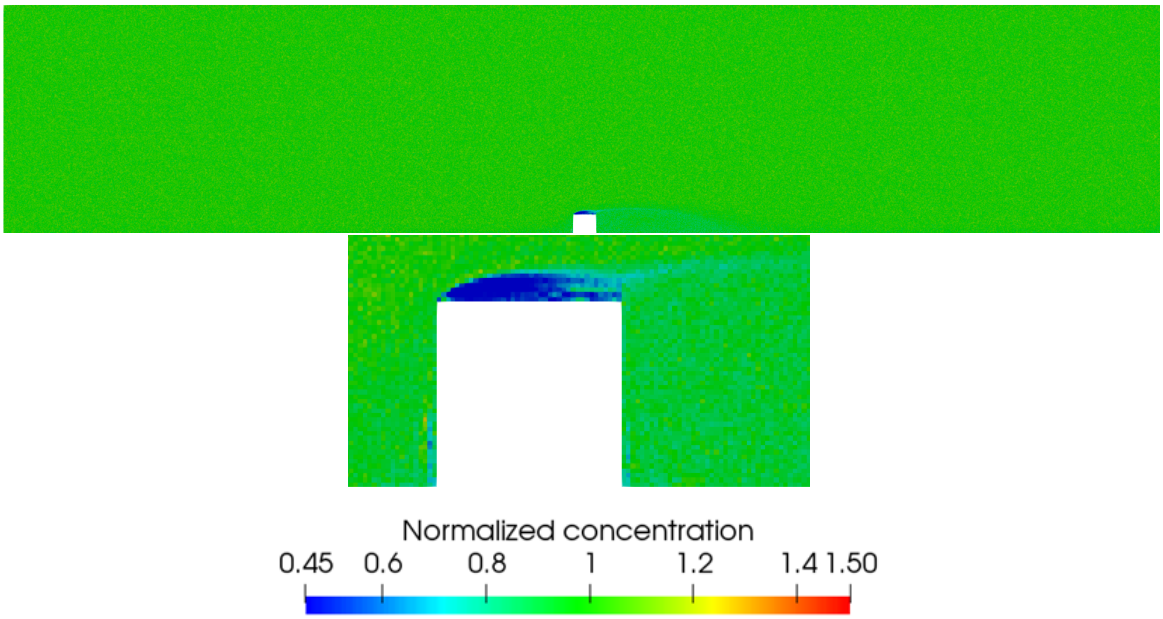

FIGURE 5.1 – Champ de concentration normalisé $c/\langle c \rangle$ pour le cas de l'obstacle au sein d'une couche limite, avec dimensions multipliées par 100, paroi rugueuse au sol et entrée au sommet. De haut en bas : vue globale, zoom autour de l'obstacle.

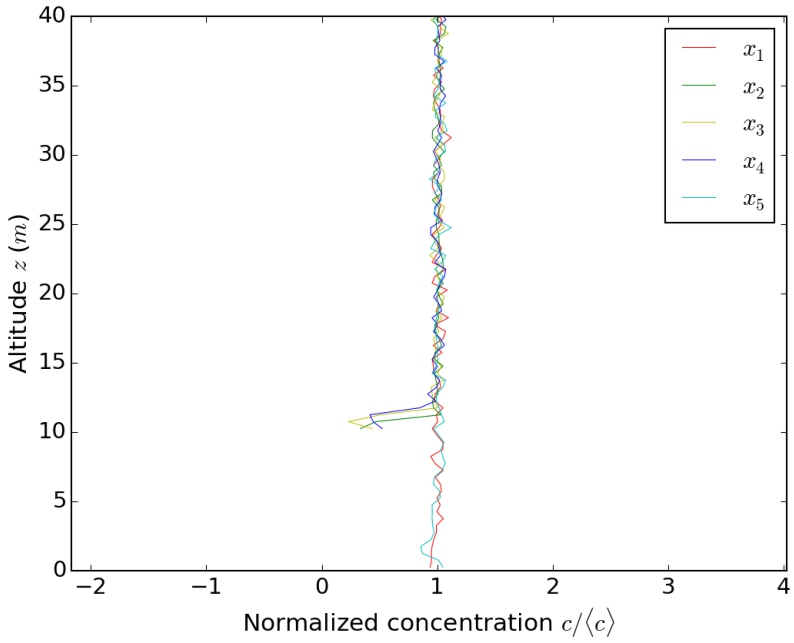

FIGURE 5.2 – Profils verticaux de concentration normalisée au niveau des cinq plans de coupe indiqués dans la Figure 15 de l'article BAHLALI et al. (2018c), pour le cas de l'obstacle au sein d'une couche limite, avec dimensions multipliées par 100, paroi rugueuse au sol et entrée au sommet.

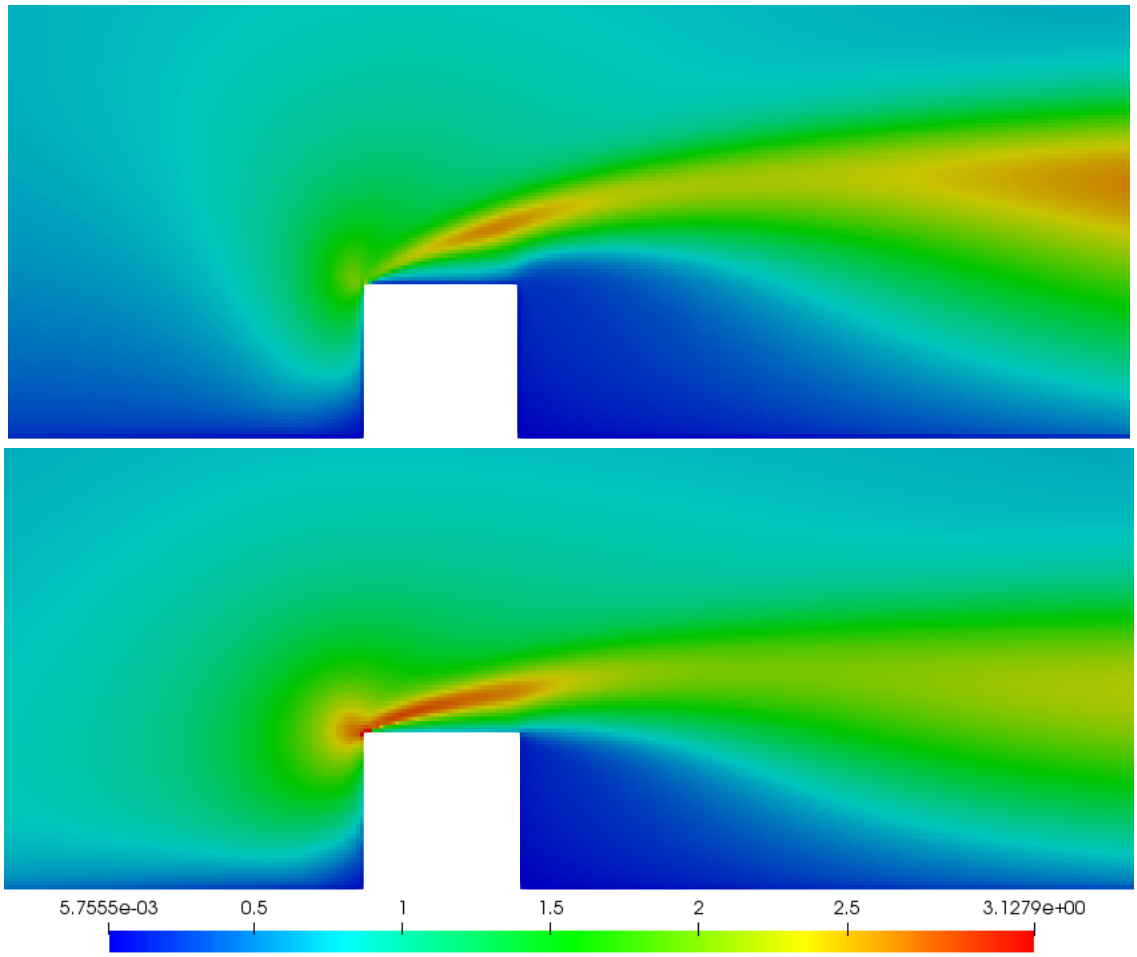

FIGURE 5.3 – Champ d'énergie cinétique turbulente pour le cas de l'obstacle au sein d'une couche limite, avec dimensions multipliées par 100, paroi rugueuse au sol et entrée au sommet. De haut en bas : $z_0 = 0.0025$ m, $z_0 = 0.1$ m.

gauche de l'obstacle et également au-dessus de celui-ci. Une analyse du déplacement des particules a permis de voir que la région où l'énergie cinétique turbulente est très importante correspond à la première région "vidée" par les particules. Il y a potentiellement une difficulté du modèle lagrangien à suivre les particules dans cette région de recirculation particulièrement complexe, accentuée en conditions rugueuses puisque la turbulence y est beaucoup plus importante. Des investigations plus approfondies sont en cours et sont à développer en perspectives de ce travail de thèse.

Enfin, de même que dans l'article Bahlali et al. (2018c), nous avons sélectionné trois zones (en amont, au-dessus, et en aval de l'obstacle), et au niveau de chacune de ces zones nous avons tracé les profils verticaux des tensions de Reynolds R_{11}, R_{33} et R_{13}. Ceci est illustré dans la Figure 5.4. Les formes des courbes sont différentes de celles présentées dans Bahlali et al. (2018c), puisque nous avons imposé au sommet une condition d'entrée afin d'avoir un flux R_{13} constant dans la couche limite considérée. En amont de l'obstacle, des écarts sont observés entre les prédictions dupliquées correspondant aux solveurs eulérien et lagrangien, en particulier en proche paroi. Nous observions un phénomène comparable dans le cas du canal plan infini de l'article Bahlali et al. (2018c), où des écarts entre les prédictions des deux solveurs étaient observés près de la paroi. En perspective, des travaux seraient donc à poursuivre sur les conditions aux limites particulaires.

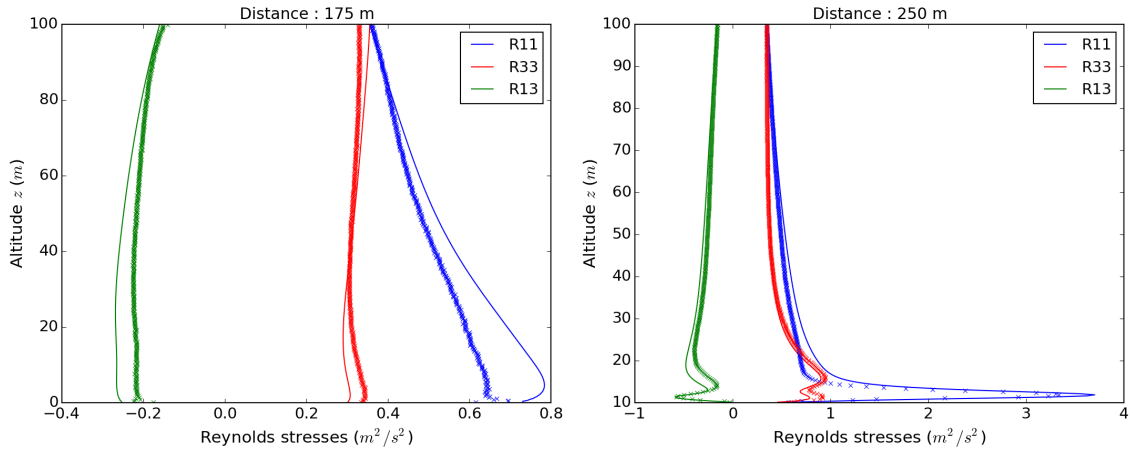

(a) En amont de l'obstacle

(b) Sur l'obstacle

(c) En aval de l'obstacle

FIGURE 5.4 – Profils verticaux des tensions de Reynolds au niveau des trois plans de coupe utilisés dans la Figure 22 de l'article BAHLALI et al. (2018c), pour le cas de l'obstacle au sein d'une couche limite, avec dimensions multipliées par 100, paroi rugueuse au sol et entrée au sommet. Les prédictions dupliquées correspondent aux résultats du solveur eulérien (lignes continues) et du solveur lagrangien (croix).